European Journal of Mechanics / A Solids 118 (2026) 106068

Contents lists available at ScienceDirect

European Journal of Mechanics / A Solids

journal homepage: www.elsevier.com/locate/ejmsol

Full length article

Experimental and numerical spatio-temporal analysis of the Portevin–Le Chatelier dynamics in a Nickel based superalloy

Florian Billon [a,b,c], Aurélien Vattré [b], Sylvain Zambelli [c], Matthieu Mazière [a], Samuel Forest [a,*]

[a] Mines Paris - PSL, Centre des Matériaux, CNRS UMR 7633, 21 Allée des Marronniers, Versailles, 78000, France
[b] ONERA, DMAS, 29 av. Division Leclerc, Châtillon, 92320, France
[c] Safran Aircraft Engines, Roind-point René Ravaud, Moissy-Cramayel, 77550, France

ARTICLE INFO

Keywords:
Portevin–Le Chatelier
Nickel based superalloy
Finite element modelling
Machine stiffness
Statistical analysis
Non-linear dynamics
Spatio-temporal instabilities

ABSTRACT

This study examines the Portevin–Le Chatelier (PLC) effect in the nickel-based superalloy Inconel 718 through a combined experimental-computational approach using statistical indicators from nonlinear dynamical systems theory. We develop a finite element model incorporating the Kubin–Estrin–McCormick constitutive law to capture Dynamic Strain Ageing effects, accounting for machine stiffness influence, and reproduce various dynamics under both hard and soft loading conditions. Statistical analysis reveals that machine stiffness significantly affects serration morphology and dynamics, influencing mean amplitudes, stress drop periods, and dynamical indicators such as the correlation dimension and Lyapunov exponents. Comparison of simulated and experimental stress time series demonstrates chaotic behaviour for type B and C serrations across all strain rates, with no evidence of self-organised criticality in experimental data. However, simulations predict self-organised criticality at high strain rates corresponding to type A bands, consistent with literature references. Statistical indicators reveal power-law behaviour for stress drop amplitudes as a function of strain rate, with critical exponents dependent on band type. Multifractal analysis shows that simulations overestimate complexity relative to experimental observations, suggesting the need for additional internal variables and finer-scale dynamics in modelling. Additionally, multifractal analysis of spatio-temporal diagrams reveals power-law distributions of plastic strain rates with consistent critical exponents across all strain rates, demonstrating its potential for characterising PLC spatio-temporal dynamics. Statistical, dynamical, and multifractal indicators show consistent correlations, collectively capturing transitions between serration regimes and serving as reliable quantitative metrics for characterising PLC dynamics. The analysis is finally applied to the spatio-temporal strain fields measured by digital image correlation. The results demonstrate the value of multi-indicator analysis for assessing the agreement between experiment and simulation and subsequently improving constitutive model parameter identification.

1. Introduction

The Portevin–Le Chatelier (PLC) effect, also known as jerky flow, is a well-known plastic instability that may occur under various deformation conditions (Kubin and Estrin, 1990; Benallal et al., 2006, 2008). Uniaxial tensile tests represent the most commonly used configuration to study this phenomenon, where it manifests as a sequence of stress drops followed by reloading, giving the stress–strain curve a characteristic serrated appearance. These stress drops are associated with the nucleation of plastic localisation bands, which may emerge randomly or propagate continuously or intermittently across the specimen. The PLC effect is commonly observed in a wide range of dilute alloys, including those with face-centered cubic (FCC) structures such as Al–Mg and Ni-based alloys, body-centered cubic (BCC) ferritic steels, and hexagonal close-packed (HCP) such as titanium alloys (Rowlands et al., 2023).

The underlying mechanism responsible for the PLC effect is Dynamic Strain Ageing (DSA), a thermally activated phenomenon involving the interaction between mobile dislocations and diffusing solute atoms in the crystal matrix. The commonly accepted interpretation, originally proposed by Van Den Beukel and Kocks (1982), considers dislocation motion as intermittent (Sleeswyk, 1958), alternating between phases of rapid glide and arrest at obstacles such as forest dislocation or precipitates. The diffusion of solute atoms towards arrested dislocations core, further pins them and promotes the intermittency of their motion. As such, dislocations can be freed from their obstacles through

* Corresponding author.
E-mail address: samuel.forest@minesparis.psl.eu (S. Forest).

https://doi.org/10.1016/j.euromechsol.2026.106068
Received 4 December 2025; Received in revised form 26 January 2026; Accepted 5 February 2026
Available online 12 February 2026

avalanche-like events, resulting in an abrupt stress drop and/or strain increment characteristic of the PLC effect.

Several diffusion modes are considered in the literature such as bulk or pipe diffusion, where in the latter, forest dislocations act as short-circuit for the diffusion of solutes towards arrested dislocations. Alternative interactions have also been proposed, including cross-core effects (Curtin et al., 2006) and solute clustering affecting junction strength (Picu, 2004). As such, during a tensile test, if solute atom diffusion time becomes comparable to the dislocation waiting time, the material exhibits Negative Strain Rate Sensitivity (NSRS) which is the necessary material property needed for the emergence of jerky flow (Penning, 1972).

Although the stress–strain response may appear erratic, the morphology of the serrations and the dynamics of the plastic localisation bands exhibit strongly different features depending on the applied strain rate. Classification distinguishes three main band types (Rodriguez, 1984). At low strain rates, C-type serrations are observed, characterised by large stress drops and the random emergence of localisation bands. At intermediate strain rates, B-type bands occur, associated with smaller stress drops and hopping band propagation. For higher strain rates, A-type bands are observed, displaying continuous propagation of plastic localisation through the specimen and small-amplitude stress oscillations at the continuum scale.

The most widely used phenomenological approach to DSA is the Kubin–Estrin–McCormick (KEMC) model (McCormick, 1988; Kubin and Estrin, 1990), which accounts for solute diffusion towards dislocations by introducing an additional hardening term that depends on an effective ageing time variable t_a. Other models have been developed, including micromechanical (Fressengeas et al., 2005; Varadhan et al., 2009; Ananthakrishna and Valsakumar, 1982) and thermodynamic formulations (Rizzi and Hähner, 2004; Zhu et al., 2024). The KEMC model has been implemented in several finite element packages and is widely used to investigate the influence of DSA on the behaviour of many structural materials (Graff et al., 2004; Mazière et al., 2010a; Zhang et al., 2001; Böhlke et al., 2009). One of the well-known features of this model is its ability to reproduce the serrated flow stress and the nucleation of plastic bands. Finite element simulations incorporating the KEMC model are now widely regarded as standard tools for modelling the PLC effect in complex structures, providing critical insights into material behaviour under complex loading conditions. This modelling approach has only recently been applied to Nickel-based superalloys (Mazière et al., 2010b; Song et al., 2020; Guillermin et al., 2023).

The occurrence of the Portevin–Le Chatelier (PLC) effect is strongly correlated with temperature, as temperature governs the kinetics of solute diffusion towards mobile dislocations. In specific regimes, this interaction can lead to an increase in flow stress with increasing temperature (Blanc and Strudel, 1985), in contrast to the conventional thermal softening typically observed in metallic materials. Such behaviour can be effectively accounted for through temperature-dependent material parameters within constitutive frameworks such as the KEMC model (Belotteau et al., 2009). Experimental investigations based on infrared pyrometry have further shown that local temperature increases of a few degrees may develop within PLC bands during deformation (Ranc and Wagner, 2005). However, the magnitude of these temperature variations, as well as their influence on the macroscopic and mesoscopic mechanical response, remain limited. As a result, they do not warrant the introduction of a more complex modelling framework involving spatially inhomogeneous temperature fields and fully temperature-dependent constitutive parameters. Consequently, temperature variations are considered negligible in the present study, and the mechanical behaviour is analysed under isothermal conditions.

The PLC effect displays rich spatio-temporal dynamics that is directly reflected in the serrated morphology of the strain–stress curve. To understand and characterise the peculiar dynamics of the PLC effect, dynamical and statistical methods, first introduced in nonlinear dynamics theories, were used to investigate the irregular behaviour of the serrations (Lebyodkin et al., 1995, 2000; Bharathi et al., 2002), and uncover the underlying order. These methods involve the reconstruction of the system attractor (Takens, 1981) and its subsequent characterisation with indicators either geometric such as the fractal dimension or dynamic like the Lyapunov exponents (Schuster, 1988). As the PLC effect is associated with a highly irregular plastic flow, the fractal dimension alone — reflecting only global scaling — cannot fully capture the system's complexity. Multifractal analysis can then be applied to capture the local variations of the scaling exponents used to describe the system (Bharathi et al., 2001; Lebyodkin and Estrin, 2005). These approaches have demonstrated the existence of two distinct dynamical regimes associated with the different serration types. At low and intermediate strain rates, corresponding to type B and C serrations, the dynamics is chaotic and involves a limited number of degrees of freedom (Ananthakrishna et al., 1995). At higher strain rates, the system transitions to a self-organised critical (SOC) regime, characterised by avalanche-like events and power-law distributions of serration amplitudes and strain increments, typical of type A serrations (Bharathi et al., 2002). While previous studies (Klusemann et al., 2015) focused on the nucleation and propagation of PLC bands, the present paper extends this work by performing a comprehensive statistical, dynamical and multifractal analysis of serrations and strain localisation patterns, providing new insights into the mesoscale dynamics of plastic flow.

Most experimental analyses of the PLC effect have focused on Al–Mg alloys, where the PLC effect occurs at room temperature, facilitating its observation and study. The next challenging step would be to use the same methodology to characterise PLC dynamics in other alloys, such as nickel-based superalloys, in order to determine if chaotic and SOC dynamics are intrinsic to the PLC effect or depend on the considered alloy in a high temperature regime. Moreover, even if the KEMC model captures many macroscopic features of the PLC effect, including NSRS and band localisation, it remains unclear whether the model is capable of reproducing the complex dynamical and statistical behaviour observed experimentally (Bharathi et al., 2002). Prior studies have explored these aspects for other models using semi-analytical formulations (Lebyodkin et al., 2000) or crystal plasticity formulations (Kok et al., 2003). However, similar analyses have yet to be extended to structural simulations.

Experimentally, a strong interplay between the testing apparatus and the dynamics of the PLC effect has been observed. Van den Brink et al. (1977) demonstrated that the period of serrations increases as the machine stiffness decreases. More recently, tests on Al–Mg alloys have shown that variations in machine stiffness can trigger transitions in serration dynamics for tensile tests at fixed cross-head velocity (Tretyakov et al., 2021). In particular, a reduction in rigidity leads to a shift from type A to type C bands and to an increase in the critical strain. These experimental findings highlight the necessity of incorporating machine stiffness into the models to achieve consistency with observations and highlight the intrinsic material behaviour (Penning, 1972; Kubin et al., 1988). The machine stiffness can be incorporated in finite element models based on several strategies proposed in the literature: the use of a variable displacement rate (Belotteau et al., 2009), the addition of elastic elements to represent the machine compliance (Wang et al., 2012), or the introduction of a spring in series with the specimen (Guillermin et al., 2023; Luo et al., 2024). Such approaches have improved the modelling of serration morphology, periods, and amplitudes (Guillermin et al., 2023), with findings indicating that increased stiffness reduces the average serration periods and amplitudes (Luo et al., 2024). Nevertheless, the impact of stiffness on statistical and dynamical indicators remains, yet, to be fully understood.

In this work, we address these gaps through a comprehensive numerical investigation of the PLC effect in the Ni-based superalloy Inconel718. The originality of this contribution lies in the systematic comparison between experimental data and finite element simulations by means of broad range of statistical spatio-temporal analysis methods.

It also presents, for the first time, the application of such statistical tools not only to global serrated stress–strain curves but also to the full spatio-temporal fields measured by DIC, along with detailed analysis of the attractors in the phase space within the framework of a cusp catastrophe, which describes how continuous variations of control parameters — here, the applied strain rate — can induce sudden, discontinuous transitions in the state of a system (Thom, 1972; Arnold, 1992). In the case of the PLC effect, this framework captures the bifurcation from stable plastic flow to jerky behaviour. The stress–strain response can then be interpreted as a folded surface, where the cusp geometry naturally accounts for the abrupt stress drops observed as the system crosses the fold, as previously pointed out by Kubin and Estrin (1985). The machine stiffness and the interaction of PLC bands with specimen boundaries are demonstrated to play a major role on the spatio-temporal dynamics of the PLC effect.

The article begins with the description of the experimental database used for identifying the model in Section 2. Then, Section 3 introduces a finite element model incorporating machine stiffness and a stabilised version of the KEMC model precluding the occurrence of PLC bands while keeping the negative strain sensitivity. In Section 4, the tools used to characterise the PLC dynamics from the simulations are described and include statistical, dynamical, and multifractal analysis methods. In Section 5, we assess the effect of the machine stiffness on the evolution of the PLC dynamics, we analyse the variation of dynamical indicators with strain rate, and compare the numerical results with experimental observations. Then, Section 6 is devoted to the discussion of the spatio-temporal dynamics of type A bands, elucidating how the interaction between propagating bands and the boundaries of the gauge section leads to macroscopic stress drops. It further demonstrates how the dynamics of the PLC effect can be characterised using the various indicators introduced throughout the study. Finally, the structure of the model phase space at a Gauss point is analysed and its evolution is correlated with the occurrence of stress drops. Section 7 concludes the study.

2. Material and experimental background

2.1. Material

The studied material is an Inconel718, a polycrystalline Nickel based superalloy developed during the 1960s, used for aeronautical applications such as turbine disks. This alloy is made of an austenitic matrix γ, consisting of a disordered solid solution of Ni with a face-centred cubic structure. Within this matrix, $\gamma' - \mathrm{Ni_3(Ti, Al)}$ and $\gamma'' - \mathrm{Ni_3Nb}$ precipitates are found, both of which prove to be essential for the structural hardening of the material, and its remarkable mechanical properties (Reed, 2006).

Some of the mechanical tests performed by Guillermin et al. (2023) are used in the present study. The specimens were sampled from a forged bar of final dimensions 117 mm in diameter and 435 mm in length. To reach the desired mechanical properties of the industrial alloy, the bar was subjected to a series of heat treatments. It was first annealed at 965 °C during one hour and then quenched to room temperature. Next, the material was aged, first held at a temperature of 720 °C for 8 h and then cooled at a rate of 50 °C/hour until it reached 620 °C. It was then further maintained at this temperature for 8 more hours, before being cooled at room temperature. To minimise the possible effect of gradients in material properties, the specimens were machined on the outer perimeter of the bar.

2.2. Tensile tests

The database used for this study has been built upon the experimental work achieved by Guillermin et al. (2023). Two geometries were designed: smooth axisymmetric (ST) and flat (D0) specimens shown in Figs. 1(a) and 1(b), respectively. All the tensile tests were performed on the same hydraulic tensile test machine equipped with a 50 kN load cell. The setup was heated to a temperature of 500 °C with a lamp oven, the temperature being controlled by a thermocouple welded at the surface of the specimen. Tests were performed under displacement controlled conditions in a range of strain rates comprised between $\dot{\varepsilon} \in \left[10^{-5}, 10^{-1}\right]\ \mathrm{s}^{-1}$.

Strain measurements for both geometries are obtained using optical methods. In the ST geometry, markers are placed along the gauge length and tracked by a camera during the tensile test; strain is then calculated from their displacements. For the D0 specimens, strain is measured using two-dimensional digital image correlation (2D-DIC). This imaging method proves to be useful to observe strain localisation phenomena as it allows for a wide field of view, with high spatial resolution and sampling rate. The strain computations of the relevant fields were then performed with the Vic-2D software. A laser engraving process was used to apply speckle patterns on specimens (Guillermin et al., 2023). This particular method proved to be resilient to high temperature and large strains, ensuring the accuracy of DIC up to the fracture of the specimen.

Results of the tensile tests are given in Fig. 1(c) for the flat specimen and Fig. 1(d) for the axisymmetric specimen. Compilation of the experiments allows observing qualitatively the NSRS as the stress decreases with strain rate. All tensile tests display serrations, defined as sudden drops of the stress during the tensile test. They appear to be more pronounced at low strain rates while their frequency increases with strain rate. A different behaviour is observed at $\dot{\varepsilon} = 10^{-1}\ \mathrm{s}^{-1}$, which may be due either to a change in the structural dynamics of the PLC effect or to experimental limitations, as the sampling rate (100 Hz) is not high enough to capture all events during the tensile test.

The comparison of Figs. 1(a) and 1(b) indicates a significant difference between the stress level at a given strain rate between the two specimen types. These differences from the fact that both specimen types were taken from two different ingots with different sampling directions. D0 specimens were cut along the longitudinal direction of the round bars, while ST specimens were cut across the transverse direction (tangential). The differences in the overall curves originate from both the variability between ingots and the anisotropy between the longitudinal and transverse directions. However, Figs. 1(a) and 1(b) show that the amplitude and periods of stress drops are similar for both types of specimens, despite the different overall stress levels.

3. Modelling of the PLC effect

This section presents the constitutive modelling approach and finite element simulation framework used to reproduce the PLC effect in Inconel 718. Two models are presented, one which describes the usual implementation of the Kubin–Estrin–McCormick model in the elasto-visco-plastic framework and an original modified KEMC model that stabilises the model and removes the possible instabilities while keeping the negative strain rate sensitivity. The latter model will be used for the identification of the hardening behaviour.

3.1. KEMC model for the Inconel 718 alloy

The most successful phenomenological model of DSA, including effects, is the Kubin–Estrin–McCormick (KEMC) constitutive law (McCormick, 1988; Kubin and Estrin, 1990). The original model was then extended to temperature and finite deformation effects in several contributions (Mesarovic, 1995; Zhang et al., 2001; Graff et al., 2004; Böhlke et al., 2009; Mazière et al., 2010a). The model is efficient enough to be applied to structural finite element simulations.

The proposed constitutive setting consists of an isotropic nonlinear elasto-visco-plastic behaviour law. For brevity, the model is presented here within the small strain framework. It is however extended to the finite deformation framework by means of the corotational formulation equivalent to the use of Jaumann objective derivatives, see Besson et al.

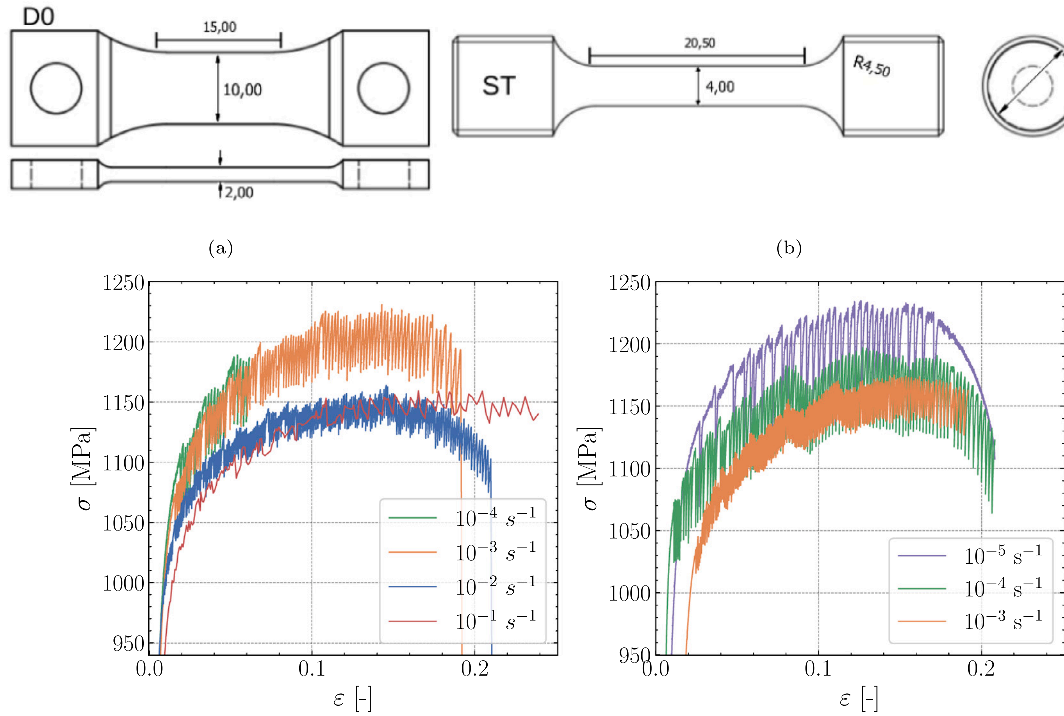

(a) (b)

(c) Flat geometry D0 (d) Axisymmetric geometry ST

Fig. 1. (a) Flat specimen geometry and dimensions, (b) Axisymmetric specimen geometry and dimensions, (c) Flat specimen engineering strain–stress curves for strain rates $\dot{\varepsilon} \in \left\{10^{-4}, 10^{-3}, 10^{-2}, 10^{-1}\right\}$ s^{-1}, (d) Axisymmetric specimen engineering strain–stress curves for strain rates $\dot{\varepsilon} \in \left\{10^{-5}, 10^{-4}, 10^{-3}\right\}$ s^{-1}. For both geometries NSRS and serrations are observed until $\dot{\varepsilon} = 10^{-1}$ s^{-1}.

(2012), Guillermin et al. (2023). All numerical simulations of the work are performed using the finite deformation formulation.

Under isothermal conditions, the total strain rate is expressed by an additive decomposition into elastic and plastic parts:

$$\dot{\underset{\sim}{\varepsilon}} = \dot{\underset{\sim}{\varepsilon}}^e + \dot{\underset{\sim}{\varepsilon}}^p \quad \text{where} \quad \dot{\underset{\sim}{\varepsilon}}^e = \underset{\approx}{E}^{-1} : \dot{\underset{\sim}{\sigma}} \tag{1}$$

where $\underset{\approx}{E}$ is the Hooke tensor of elasticity. The evolution of plastic strain is determined by the yield function f and the plastic flow rule:

$$f\left(\underset{\sim}{\sigma}, p, t_a\right) = \bar{\sigma} - R_h(p) - R_a\left(p, t_a\right) \quad \text{and} \quad \dot{\underset{\sim}{\varepsilon}}^p = \dot{p}\frac{\partial f}{\partial \underset{\sim}{\sigma}} \tag{2}$$

where $\bar{\sigma}$ is an equivalent stress measure, R a non-linear strain hardening law, R_a accounts for the contribution of DSA to the yield stress, and p, t_a are internal variables defined in the sequel. The Hosford equivalent stress measure is adopted (Hosford, 1972):

$$\bar{\sigma} = \frac{1}{2^{1/n}}\left(\left|\sigma_I - \sigma_{II}\right|^n + \left|\sigma_{II} - \sigma_{III}\right|^n + \left|\sigma_{III} - \sigma_I\right|^n\right)^{1/n} \tag{3}$$

where $\sigma_I \geq \sigma_{II} \geq \sigma_{III}$ are the principal stresses. The parameter n is a material-dependent exponent adjusting the shape of the yield surface. Von Mises and Tresca criteria are recovered for $n = 2$ and $n = \infty$ respectively. The cumulative plastic strain rate $\dot{p}$ is computed using a viscoplastic flow rule:

$$\dot{p} = R_v^{-1}(\langle f \rangle), \quad \langle f \rangle = \max(0, f) \tag{4}$$

where R_v is the inverse of any classical flow law, here chosen as a hyperbolic sine law:

$$R_v(\dot{p}) = K \sinh^{-1}\left(\frac{\dot{p}}{\dot{p}_0}\right) \tag{5}$$

The equivalent plastic strain, p, is then computed as the time integration of $\dot{p}$, with the initial condition $p(0) = 0$.

Isotropic hardening is described by the following non-linear strain hardening law:

$$R_h(p) = R_0 + \sum_{i=1}^{2} Q_i\left(1 - \exp(-b_i p)\right) \tag{6}$$

where R_0 is the initial yield strength, while Q_i and b_i are material properties to be identified. As proposed in Eq. (2), the DSA contribution is taken as an isotropic hardening term R_a, which is a function of cumulative plastic strain p and the ageing time variable t_a:

$$R_a\left(p, t_a\right) = P(p)\left(1 - \exp\left(-P_2 t_a^{\beta}\right)\right) = P_1\left(c_1 + c_2 p\right)\left(1 - \exp\left(-P_2 t_a^{\beta}\right)\right) \tag{7}$$

The term $P(p) = P_1\left(c_1 + c_2 p\right)$ is a stress factor representing the resistance exerted by solutes on dislocation glide motion. It sets the maximum possible value of the stress serration amplitude. It depends on the strain hardening effect associated with dislocation density evolution (Zhang et al., 2001; Böhlke et al., 2009). The kinetic rate of diffusion is controlled by P_2 and β. Commonly used values for β are either 0.33 or 0.66 which account for pipe or bulk diffusion respectively (Graff et al., 2008). The evolution of ageing time t_a is controlled by a Boltzmann-type relaxation law (McCormick, 1988):

$$\dot{t}_a = 1 - \frac{t_a}{w(p)}\dot{p} = 1 - \frac{t_a}{w_1 + w_2 p}\dot{p} \tag{8}$$

with the initial condition $t_a(t = 0) = t_a^0$.

Three specific regimes should be underlined:

- $\dot{p} \to 0$: dislocations are at rest, equivalent to $\dot{t}_a = 1$. The ageing time coincides with physical time and the solute concentration at the dislocation cores increases.
- $\dot{p} = w(p)/t_a$: stationary regime for which $\dot{t}_a = 0$.
- $\dot{p} \to \infty$: dislocations are moving fast, equivalent to $\dot{t}_a = -t_a\dot{p}/w(p)$. Dislocations are unpinned from the solute atmospheres and the solute concentration at the dislocation core drops.

Table 1
Hardening law, viscosity, and dynamic strain ageing parameters for Inconel718 at 500 °C (Guillermin et al., 2023).

E [MPa]	R_0 [MPa]	Q_1 [MPa]	b_1 –	Q_2 [MPa]	b_2 –	$\dot{p}_0$ [s^{-1}]	K [MPa]	n –
188000	684	256	215	579	7.37	10^{-8}	5.67	8
P_1 [MPa]	P_2 [s^{-1}]	c_1 –	c_2 –	α_p –	β –	ω_1 –	ω_2 –	
1.00	1.15	102.00	878.00	0.00	0.33	1.45×10^{-4}	10^{-5}	

In the relaxation Eq. (8), the parameter w is related to the increment of plastic deformation carried by the PLC bands (Kubin and Estrin, 1990). In this model, both w and the stress factor P are set to depend on the cumulative plastic strain, in order to take into account work-hardening effects on the ageing dynamics (Zhang et al., 2001; Böhlke et al., 2009; Ren et al., 2017). The model parameters were previously identified by Guillermin et al. (2023) following a sophisticated identification strategy not detailed here. They are given in Table 1. The model parameters were calibrated using the D0 data, as the DIC measurements enabled us to identify the plastic strain carried by PLC bands. However, the simulations presented in this work only deal with the D0 specimens due to the long computation times associated with tiny time steps (with minimal values of 1.25×10^{-5} s).

3.2. Stable DSA model

For this study, a stabilised version of the KEMC model is introduced. The purpose of this model is to suppress PLC instabilities, while maintaining the negative strain rate sensitivity (NSRS) and hardening behaviour. It allows running elasto-viscoplastic structural simulations incorporating DSA effects without simulating serrations nor PLC bands as their computation is time expensive. As such it significantly decreases computation time. This model will be used in the following as reference serration-free model incorporating NSRS.

Such a stabilised PLC model was proposed by Zhang et al. (2012). It consists of generalising Eq. (8), by introducing a power law of the form:

$$\dot{t}_a = 1 - \left(\frac{t_a\dot{p}}{w}\right)^{\eta} \tag{9}$$

where η is an exponent chosen to be significantly smaller than unity, in order to dampen the transient response to a perturbation of the strain rate. As such, it avoids the emergence of strain rate localisation and stabilises the model. However, this approach has drawbacks: it alters the core behaviour of the original KEMC model, potentially modifying the hardening and viscoplastic response of the model and introducing a new stabilisation parameter that must be calibrated for each application.

In the present work we propose a novel stabilisation strategy which differs from the one of Zhang et al. (2012). The primary concept is to detect the emergence of an instability by a suitable perturbation analysis and then modify specific parameters within the set of equations to inhibit the triggering of plastic strain rate localisation. The onset of PLC is identified by means of the stability criterion of Mazière and Dierke (2012). The criterion initially aims at determining the critical plastic strain ε^c, at which the first serration can appear. To do so, two criteria were identified through a bifurcation analysis of the present model set of equations: the Oscillatory Growth Criterion (OGC) and the Exponential Growth Criterion (EGC). The mathematical developments for their identification are given in Appendix. They are expressed as:

$$\begin{cases} S_{OGC} = S + \omega\Theta < 0 \\ S_{EGC} = S + \omega\Theta + 2\sqrt{\omega\Theta S_i} < 0 \end{cases} \quad\text{and}\quad \begin{cases} S = \left.\dfrac{\partial\sigma}{\partial\ln(\dot{p})}\right|_p, & \Theta = \dfrac{dR}{dp} + \dfrac{\partial R_a}{\partial p} \\ S_i = \dot{p}\dfrac{dR_v}{d\dot{p}}, & S_a = -t_a\dfrac{\partial R_a}{\partial t_a} \end{cases} \tag{10}$$

where S corresponds to the steady state Strain Rate Sensitivity (SRS). In the case where the ageing variable (t_a) is saturated, the steady state SRS can be expressed as $S = S_i + S_a$ where S_i and S_a are respectively the instantaneous SRS and ageing SRS. Θ corresponds to work-hardening modulus. All sensitivities and moduli are expressed in MPa. Another expression of the EGC consists of the combined two inequalities:

$$\left(S_{\mathrm{OGC}}\right)^2 - 4w(\Theta-\sigma)S_i < 0 \quad\text{and}\quad S_{\mathrm{OGC}} < 0 \tag{11}$$

The OGC and the EGC represent, respectively, the onset of oscillatory and exponential growth of a perturbation introduced into the constitutive equations. Numerical investigations by Mazière and Dierke (2012), as well as insights from Eq. (11), have shown that the OGC is activated before the EGC, such that $\varepsilon^c_{OGC} < \varepsilon^c_{EGC}$, where ε^c_{OGC} and ε^c_{EGC} denote the critical plastic strains associated with each type of instability. Because the EGC only allows positive plastic strain increments, it imposes a stricter condition than the OGC, which can tolerate negative increments of p. The latter is forbidden in plasticity theory and leads instead to elastic unloading.

To stabilise the constitutive equations and recover the NSRS, we leverage the fact that OGC and EGC are activated at different levels of accumulated plastic strain—provided the deformation remains homogeneous (Mazière and Dierke, 2012). The goal is to allow OGC activation, which signals the onset of NSRS influence on the plastic flow, without triggering actual localisation. Localisation (i.e., band formation) is only permitted when the plastic strain exceeds the EGC threshold. Thus, the simulation parameters must be chosen to keep the system sufficiently distant from EGC activation. The proposed strategy is to maintain the system near the OGC activation point. For that purpose, we introduce the modified relaxation law Eq. (8):

$$\dot{t}_a = \frac{w - t_a\dot{p}}{w_s} \tag{12}$$

including a new parameter w_s whose initial value is $w_s := w$ for which the initial relaxation equation, Eq. (8), is recovered. Once OGC is reached, stabilisation is enforced by updating the value of parameter w_s:

$$w_s = \frac{S_i + S_a}{\Theta} \tag{13}$$

Its value is modified in order to maintain the condition $S_{OGC} = 0$ thus postponing the fulfilment of the EGC. The repeated updates of w_s stabilise the model and ensure that the plastic strain rate will not localise.

For the aim of this study, the stabilised model is used to extract the general hardening out of the stress strain curve simulated with the KEMC model. It allows the isolation of the serrations and the subsequent study of their dynamics.

3.3. Simulation of the PLC effect

The previous model is implemented in the finite element software Zset Software. Numerical integration of the constitutive equations is performed by a Newton implicit scheme, with automatic time substepping. When divergences of the local Newton integration occur, a switch to a fourth order Runge–Kutta with automatic time adaption is performed according to Mazière et al. (2010a). Note that the FE simulations are performed under quasi-static equilibrium thus excluding

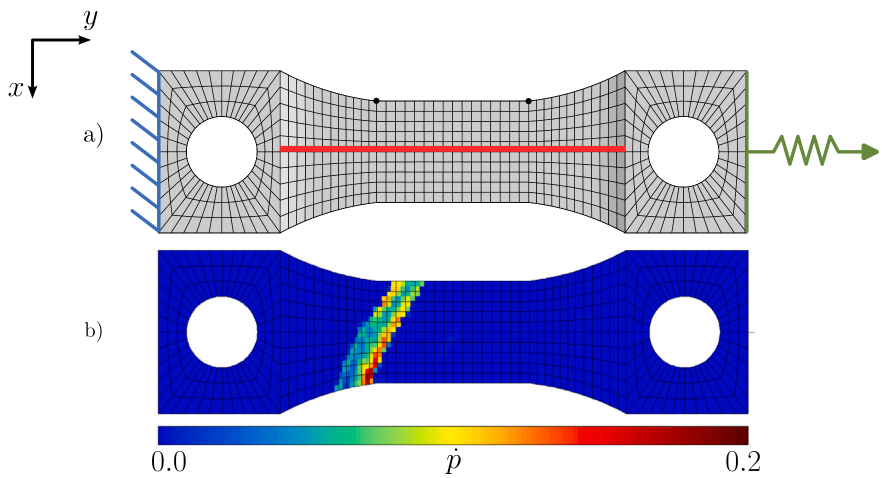

Fig. 2. (a) Finite element mesh of the flat specimen (D0). Displacement is blocked on the left end and a horizontal displacement is applied on the spring attached to the right end. The red line corresponds to the set of Gauss points used to construct the spatio-temporal diagrams in Section 5.3. The two black dots are used for extensometry. (b) Example of a localisation band depicted by the plastic strain rate for an applied strain rate $\dot{\varepsilon} = 10^{-4}$ s^{-1}. (For interpretation of the references to colour in this figure legend, the reader is referred to the web version of this article.)

inertia term from the analysis. The word "dynamics" does not refer here to elastic waves but to the nonlinear dynamical system of the KEMC constitutive equations. Consideration of inertial effects is possible but does not bring significant modification of the results given the range of investigated strain rates (Mazière et al., 2009).

Simulations were all performed on the flat specimen geometry (D0) displayed in Fig. 1(a). Mesh and boundary conditions are shown in Fig. 2. The specimen has been meshed with quadratic brick elements with reduced integration (20 nodes and 8 Gauss points). There are five elements in the thickness of the mesh of the gauge length (not shown). Although the mesh appears coarse, Mazière et al. (2010a) demonstrated that, even for coarse discretisations, the general shape of serrations remains largely mesh-independent. While exact numerical solutions may differ, the frequency and amplitude of the oscillations are consistent across different mesh densities. In the present study, we performed a comparison using a finer mesh and found no significant differences in the evolution of the serration indicators. To replicate experimental conditions, the displacement component u_y along the y-axis is fixed at the left end of the specimen, while at the right end, a Multi-Point Constraint (MPC) enforces equal displacement u_y for all nodes and is connected to a linear spring to model the machine stiffness in series with the specimen. On both sides, the displacement components u_x and u_z are set to zero (clamping conditions). The identification procedure of the machine stiffness is detailed in Section 5.2. To replicate experimental conditions, displacement is applied to the right end of the spring at a fixed velocity, chosen to match the imposed strain rate. Strain is measured by a virtual extensometer, consisting of two points at the ends of gauge section indicated by two black dots in Fig. 2.z Finally, a set of Gauss points, represented by the red line in Fig. 2, are chosen along a line spanning across the gauge and fillets, to record the plastic strain $\dot{p}$ and construct spatio-temporal diagrams. All simulations were performed on an Intel Xeon E5-2650 processor with 24 available threads. The full model was run using 12 threads, whereas the stable model required only 4.

Simulations performed with the finite element model predict the formation of plastic strain rate localisation bands as illustrated in Fig. 2b. The corresponding stress–strain curves carried out at strain rates $\dot{\varepsilon} \in \left\{10^{-4}, 10^{-3}, 10^{-2}\right\}$ s^{-1}, are displayed in Fig. 3. The dynamic behaviour of the full KEMC model can be appreciated in Video 1. The model successfully reproduces the serrations, including stress drops of magnitude in agreement with the experiments, in particular at low strain rates, as shown in Figs. 3(a) and 3(b). As observed in the simulation, the complex spatio-temporal dynamics is well reproduced by the model: type A,B and C bands dynamics is observed, each associated to its distinct morphology of serrations:

- $\dot{\varepsilon} = 10^{-4}$ s^{-1} - *type C* bands: randomly nucleated static bands associated with sharp stress drops of significant amplitude.
- $\dot{\varepsilon} = 10^{-3}$ s^{-1} - *type B* bands: hopping bands associated with sharp stress drops of smaller amplitude.
- $\dot{\varepsilon} = 10^{-2}$ s^{-1} - *type A* bands: continuously moving bands associated with small stress oscillations.

As shown in the movies, the bands propagate well into the fillets of the specimen, showing the existence of a prominent interaction of the plastic localisation with the specimen's geometry. NSRS is also recovered, as the general stress level decreases with strain rate.

Series of simulations were also performed with the stabilised model introduced in Section 3.2. The results of these simulations are also displayed in Fig. 3, along with the full model simulations. The stabilised model successfully captures the hardening behaviour of the material, and also the NSRS, while preventing the emergence of serrations. For all the considered strain rates, the evolution of w_s is displayed in Fig. 3(d). Its value increases during the simulation. As such it compensates the $t_a\dot{p}$ term in Eq. (8) and ensures that the material keeps ageing. As shown in Table 2, the stabilised model reduces computation time by approximately two orders of magnitude compared to the full KEMC model, making it significantly more efficient for simulations where serration dynamics is not required.

4. Statistical tools for the analysis of the PLC effect

The plastic flow in a tensile specimen in the PLC domain is characterised by highly complex dynamics. At first glance, jerky flow appears to be random but, its behaviour appears to be heavily dependent on temperature, strain rate and specimen's geometry (Rodriguez, 1984). This suggests that the apparent randomness of the PLC effect could be the result of the purely deterministic evolution of the underlying dynamical system. Starting in the 1980s, the analysis of the PLC effect has been carried out in the scope of non-linear dissipative systems' theory, in order to reveal the underlying mechanisms of the PLC effect and to provide a set of tools to quantify its complex dynamics (Ananthakrishna and Valsakumar, 1982; Ananthakrishna et al., 1995; Bharathi et al., 2002). It has been shown that two distinct dynamical regimes can be identified in the case of the Portevin–Le Chatelier (PLC) effect, depending on the type of deformation band involved. Type B and C bands are associated with chaotic dynamics, whereas type A bands exhibit

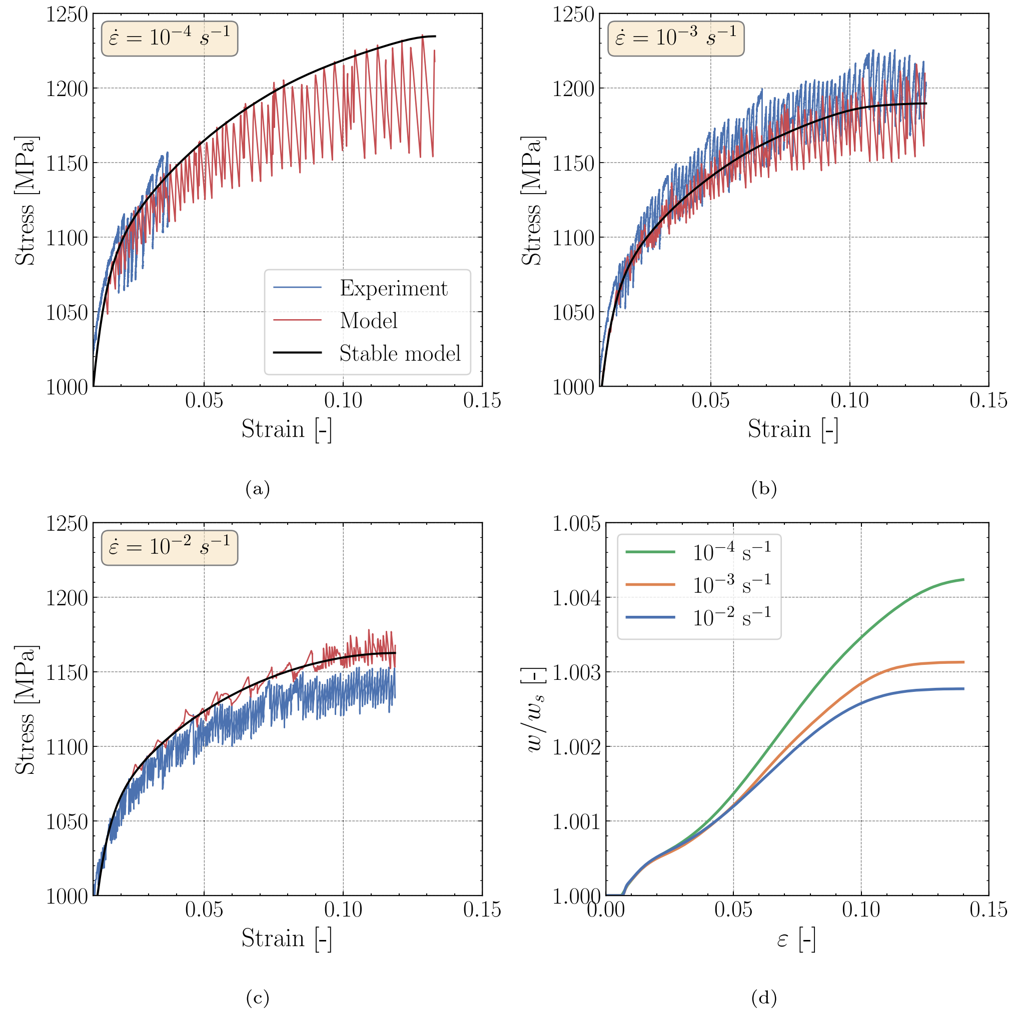

Fig. 3. Comparison between experimental data (blue), the simulated KEMC model (red), and the stabilised model (black) for the flat specimen geometry (D0) at strain rates of (a) 10^{-4} s^{-1}, (b) 10^{-3} s^{-1}, and (c) 10^{-2} s^{-1}. Negative strain rate sensitivity is captured by both the stable and full KEMC models. The stabilised model reproduces the overall hardening behaviour without serrations. The simulations show that the dynamics of serrations is consistent with experimental observations at low strain rates. (d) Evolution of the w_s parameter during a simulation using the stabilised model, showing its increase to maintain stability. (For interpretation of the references to colour in this figure legend, the reader is referred to the web version of this article.)

Table 2
Comparison of simulation CPU time for the full KEMC model and the stabilised model at different strain rates. The use of the stabilised model significantly reduces computation time by suppressing serrations while preserving overall hardening behaviour strain rate sensitivity.

Strain rate [s^{-1}]	Simulation time (full KEMC model) [s]	Simulation time (stable DSA model) [s]
10^{-4}	$2.22 \cdot 10^5$	$4.43 \cdot 10^3$
10^{-3}	$2.75 \cdot 10^5$	$4.86 \cdot 10^3$
10^{-2}	$1.24 \cdot 10^5$	$4.32 \cdot 10^3$

self-organised behaviour characterised by signatures typical of Self-Organised Criticality (SOC) (Bak et al., 1988). This specific dynamics refers to a class of dynamical systems that naturally evolve towards a critical state without external tuning, where scale-free fluctuations and power-law statistics emerge as a consequence of long-range correlations and collective interactions. As such, the use of the correct indicator allows one to identify the underlying mechanisms of the PLC effect and develop models in capacity to capture the intrinsic complexity of the PLC effect.

4.1. Detection and normalisation of serrations

During a strain-controlled tensile test, the stress–strain curve typically exhibits repeated sequences of load increase followed by a sudden stress drop. These drops, referred to as serrations, are characteristic of the PLC effect and are illustrated in Fig. 4(a). To conduct a meaningful analysis of their properties and statistical behaviour, a clear definition of what constitutes a serration is essential.

As shown in Fig. 4(a), a serration is defined as a localised stress drop, quantified by the difference between the maximum and minimum stress values within a single event: $\Delta\sigma = \sigma_{\max} - \sigma_{\min}$. Serrations are identified by scanning the stress–strain (or stress–time) signal for local maxima. For each maximum, the following minimum stress value is found before the next peak, and their difference gives the amplitude of the serration. In addition to amplitude, the period between two successive events is recorded. This period can be measured either as elapsed time τ or, preferably, as a strain increment $\Delta\epsilon$, which allows consistent comparisons across different strain rates. As illustrated in

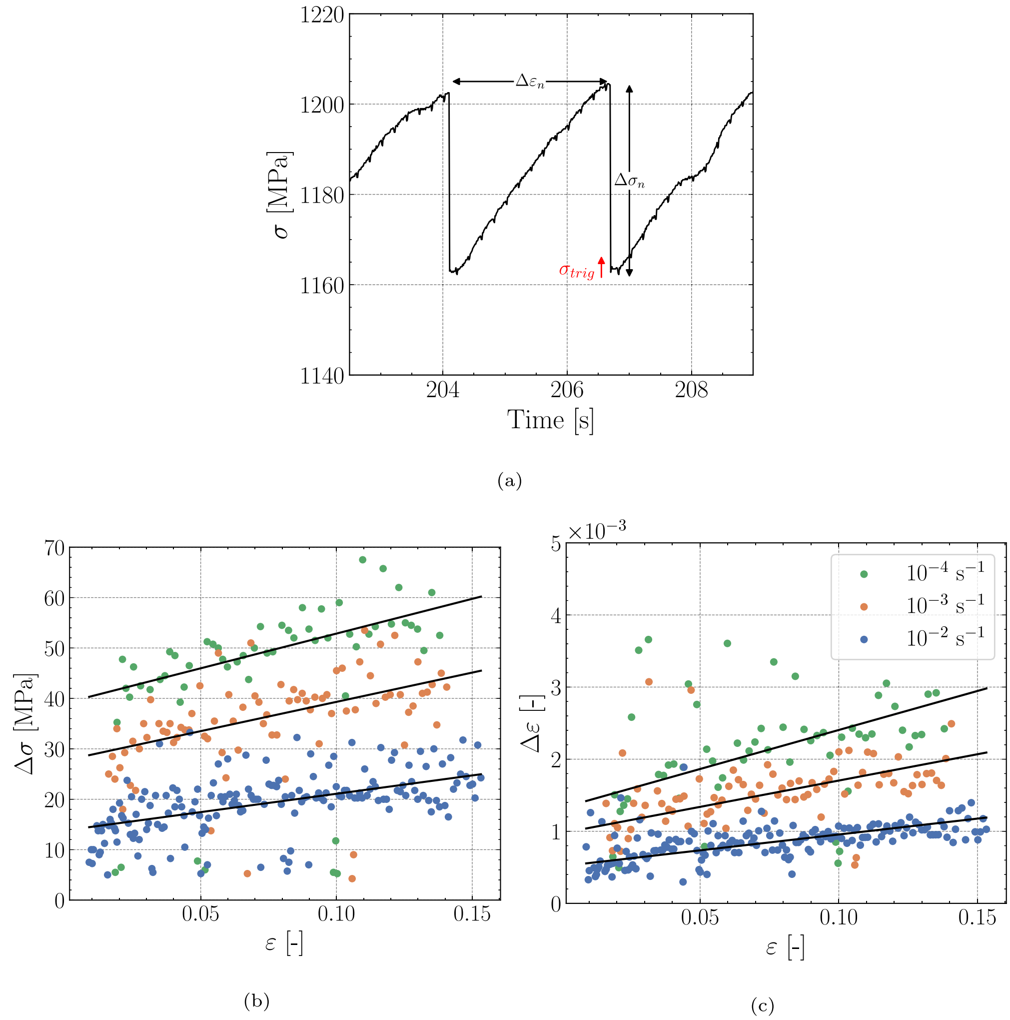

Fig. 4. (a) Time sequence of the stress and plastic activity for a strain rate $\dot{\varepsilon} = 10^{-3}$ s^{-1}. High plastic activity is observed at the onset of serrations. (b) Evolution of the amplitudes of serrations in function of the strain for a flat specimen (D0) (c) Evolution of the periods of serrations in function of the strain for a flat specimen (D0). Amplitudes and periods increase with strain while they decrease with strain rate.

Fig. 4(a), each stress drop is associated with the preceding interval, under the assumption that the serration results from the mechanical processes occurring during the reloading phase.

Smaller stress drops can be observed on the stress–strain curve. The events can either be attributed to noise, or physical events related to strain ageing happening on a much smaller spatial scale than those responsible for the big serrations. As such, special attention has to be paid to experimental signals in order to limit the influence of these events, whose physical origin is unclear. To this end, we have chosen to apply a threshold on the measured amplitudes of serrations. Based on the noise recorded during tensile experiments done at room temperature, we have set $\Delta\sigma_{trig} = 4$ MPa, see Fig. 4(a).

Once all the serrations are recorded, their amplitudes and periods are plotted in function of the strain in Figs. 4(b) and 4(c). Both amplitudes and periods increase with strain during tensile tests. It is a well known effect, associated to strain enhanced diffusion, accelerating the kinetics of diffusion, and increase of dislocation density, the combination of which strengthens the effects of DSA (Ling and McCormick, 1993). Moreover, serration amplitudes and periods decrease with increasing strain rate. This is expected, since longer time scales involved at low strain rates allow for more dislocations to get pinned. Accordingly, at the onset of a serration, more dislocations are unpinned during the avalanche process, resulting in a greater plastic strain increment and more intense stress drops.

To analyse the dynamical properties of serrations independently of microstructural effects — which cause the amplitudes to evolve with strain as seen in Fig. 4(b) — we follow the approach described in Lebyodkin et al. (1995) and Lebyodkin and Estrin (2005). First, general hardening is subtracted from the tensile curves to isolate the serrations, which are the primary focus of this study. Two distinct procedures are employed, depending on the nature of the data source: for experimental signals, a moving average filter is used to smooth the curve and remove the general hardening trend; for simulated curves, the stable model is used as a reference to subtract the hardening component, thereby avoiding the bias introduced by the choice of filtering window size. Then, a linear regression is performed on the detected serration amplitudes, $\overline{\Delta\sigma} = f(\varepsilon)$, to capture their strain dependence. The stress signal is subsequently normalised by this regression, yielding $s = \sigma / f(\varepsilon)$, which allows for consistent analysis of serration dynamics across the entire strain range.

4.2. Reconstruction and characterisation of the attractor

The apparent randomness observed in time series can, in some cases, originate from the deterministic evolution of a system—a phenomenon commonly referred to as deterministic chaos (Schuster, 1988; Strogatz, 2019). Such system evolves in a d-dimensional phase space and, due to its dissipative nature, the trajectories asymptotically contract towards a geometrical object called the attractor. This attractor emerges from the continuous stretching and folding of the system's orbits (Schuster, 1988). A hallmark of chaotic behaviour is sensitive to initial conditions, which leads to a progressive loss of memory of the system's starting state. The evolution of neighbouring trajectories is quantified by the *Lyapunov exponents*, which measure exponential divergence or convergence rates along different directions in phase space. Positive exponents describe the stretching observed in certain directions and are a typical signature of chaotic behaviour. Meanwhile, dissipation ensures contraction in other directions (associated with negative exponents), causing the overall phase space volume to decrease. The combined effect of stretching and folding organises the system's trajectory into a strange attractor—a self-similar, fractal structure characterised by a dimension D_f.

In practice, direct reconstruction of the attractor from experimental data is generally not possible, as we do not have access to all the physical parameters of the system. However, a reconstruction of the system's multidimensional dynamics from a one-dimensional experimental time series is feasible, provided the series is sufficiently long. According to Takens' theorem (Takens, 1981), the reconstructed space — called the *embedding space* — possesses similar geometrical properties to those of the original phase space.

The reconstruction starts from the experimental time series $\left(\sigma_k\right)_{1\le k\le N}$, where k is in units of the sampling time and N is the total number of sampling points. This scalar sequence is unfolded into a d-dimensional space by constructing $N-(d-1)\tau$ vectors:

$$\vec{\xi}_k = (\sigma_k, \sigma_{k+\tau}, \sigma_{k+2\tau}, \dots, \sigma_{k+(d-1)\tau}), \quad 1 \le k \le N-(d-1)\tau \tag{14}$$

where τ is the time delay, d is the embedding dimension, and $\vec{\xi}_k$ represents a point on the reconstructed trajectory in the embedding space. These points are typically arranged into a trajectory matrix $\mathbf{T}$ of size $m\times d$, where $m = N-(d-1)\tau$. Each line of the matrix $\mathbf{T}$ corresponds to a point $\vec{\xi}_k$ of the attractor.

A key issue in the reconstruction of the attractor is the identification of an appropriate time delay and embedding dimension. Although no direct method exists to determine the optimal parameters, it is possible to infer the minimum embedding dimension using the method proposed by Cao (1997). A consistent minimal embedding dimension of $d_0 = 8$ was identified across all tensile tests and is used in the reconstruction of the attractors.

The orbits of the dynamical system are not directly accessible from the trajectory matrix. To identify the subspaces where the dynamics predominantly unfold, we apply the Singular Value Decomposition (SVD), as proposed by Broomhead and King (1986). The SVD factorises the trajectory matrix as $\mathbf{T} = \mathbf{U}\mathbf{S}\mathbf{C}^T$, where $\mathbf{U}$ is an $m\times d$ matrix of left singular vectors, $\mathbf{C}$ is a $d\times d$ matrix of right singular vectors (i.e., an orthonormal basis), and $\mathbf{S}$ is a diagonal matrix containing the singular values in decreasing order.

This decomposition gives an orthonormal basis $\mathbf{C} = (\vec{c}_1, \vec{c}_2, \dots, \vec{c}_d)$ onto which the trajectory matrix $\mathbf{T}$ can be projected. The projection de-correlates the components of the trajectory, allowing to unravel the distinct dynamics of each mode. Moreover, the singular values in $\mathbf{S}$ can be used to reduce noise: by retaining only the components associated with the largest singular values, one can suppress the contribution of lower-energy modes typically attributed to noise. This approach isolates the dominant modes of the nonlinear system.

To reconstruct the attractor, we project the trajectory matrix onto the first three principal directions $(\vec{c}_i)_{1\le i\le 3}$, for practical considerations, and also, because they capture the dominant modes of the dynamical system (Kok et al., 2003). Fig. 5(a) displays the resulting attractor for a tensile test on the flat geometry at a strain rate $\dot{\varepsilon} = 10^{-3}$ s^{-1}.

Two prominent features emerge. The first is an almost vertical segment representing the loading phase. This is followed by a large loop, corresponding to a stress drop associated with a serration event. Additionally, smaller loops are scattered throughout the loading phase. These may arise from experimental noise or reflect localised plastic events triggered by DSA. The latter could either correspond to fluctuations caused by noise, or to strain bursts occurring in favourably oriented grains and grain boundaries, but with insufficient intensity to drive macroscopic propagation.

The fractal nature of the attractor is commonly quantified by the fractal dimension D_f, which can be estimated using the box-counting method. However, due to its computational cost, a more practical alternative is the computation of the correlation dimension, as proposed by Grassberger and Procaccia (1983). This method is based on the computation of the correlation integral $C(r)$, discretised and defined as:

$$C(r) = \frac{1}{N_p}\sum_{i\neq j} H\left(r - \left|\vec{\xi}_i - \vec{\xi}_j\right|\right) \tag{15}$$

where $H(\cdot)$ is the Heaviside step function, which counts the number of pairs of points $\vec{\xi}_i$ and $\vec{\xi}_j$ separated by a distance less than r, and N_p is the number of points in the time series. The self-similar structure of the attractor is reflected in the power-law behaviour of the correlation integral at small scales, where $C(r) \propto r^\nu$ and ν is the correlation dimension. The exponent ν is estimated via linear regression on a log–log plot of $C(r)$ versus r, as shown in Fig. 6(a). The smallest integer larger than $\nu+1$ is correlated to the minimal number of dimensions needed to construct the attractor phase space (Bharathi et al., 2002).

Accurate dimension computation requires selecting an appropriate regression range. Due to experimental data limitations, evaluating the correlation integral at very small r values is impractical, as the discrete data is susceptible to noise. This can be mitigated using SVD decomposition, where we only keep the principal modes to perform the computation of the dimension. Then, regression is performed over intermediate length scales to capture the fractal behaviour while minimising noise. The correlation dimension stabilises as the embedding dimension increases, as shown in Fig. 6(a).

To further characterise the nature of the attractor, we compute the Lyapunov exponents, which quantify the sensitivity of the system to initial conditions. They are typically calculated using the algorithm by Eckmann et al. (1986-12-01), which estimates the full spectrum of exponents for a system with a given number of degrees of freedom. However, this method requires long, noise-free time series, which is often impractical for experimental data. In this study, we only compute the Largest Lyapunov Exponent (LLE), noted λ_m, using the method proposed by Rosenstein et al. (1993), which is more robust to short and noisy datasets. The LLE measures the average logarithmic divergence of initially close trajectories, and is estimated from the slope of the divergence curve, as shown in Fig. 6(b). Positive Lyapunov exponents are generally considered as good indicators of the chaotic nature of a signal, as they are representative of the stretching experienced by attractor under the action of the flow (Schuster, 1988).

4.3. Multifractal analysis

In cases where the orbits of the attractor visit regions of the phase space with non-uniform frequency, or when local physical properties fluctuate, the fractal dimension alone becomes insufficient to fully characterise the system's complexity, as it only captures global scaling behaviour. To address this difficulty, Frisch and Parisi (1980) introduced the concept of *multifractality*, which describes systems with locally varying scaling exponents. Multifractality has been applied to a wide range of problems involving complex signals and patterns, with the aim of uncovering the hidden order underlying their dynamics. This includes fields such as hydrodynamic turbulence, financial time series, heart rate variability, internet traffic, and texture classification (Abry et al., 2012; Wendt et al., 2009). Multifractal analysis provides a powerful framework for characterising signal complexity, enabling both model refinement and predictive insight. In the context of the PLC effect, this approach has been employed to characterise the morphology

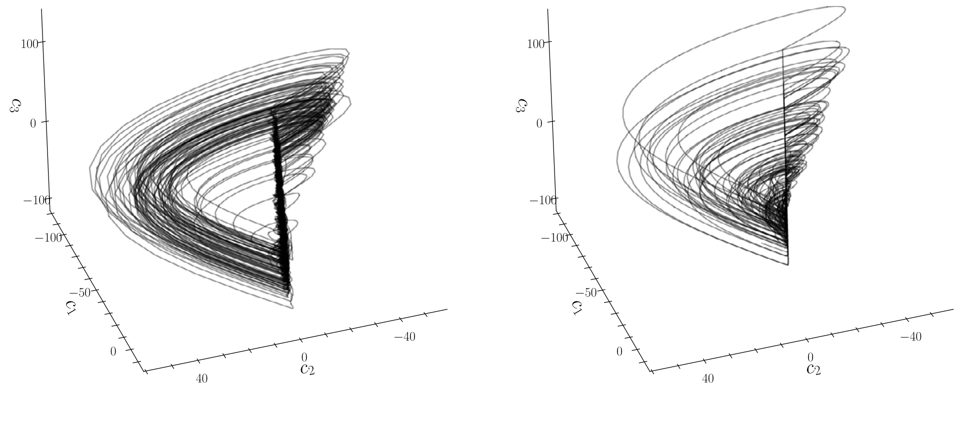

(a) (b)

Fig. 5. Reconstructed attractors of the PLC effect for (a) experimental data and (b) simulation at a strain rate of $\dot{\varepsilon} = 10^{-3}$ s^{-1}. Vertical straight segments correspond to the elastic reloading phases, while curved lines represent the stress drop events.

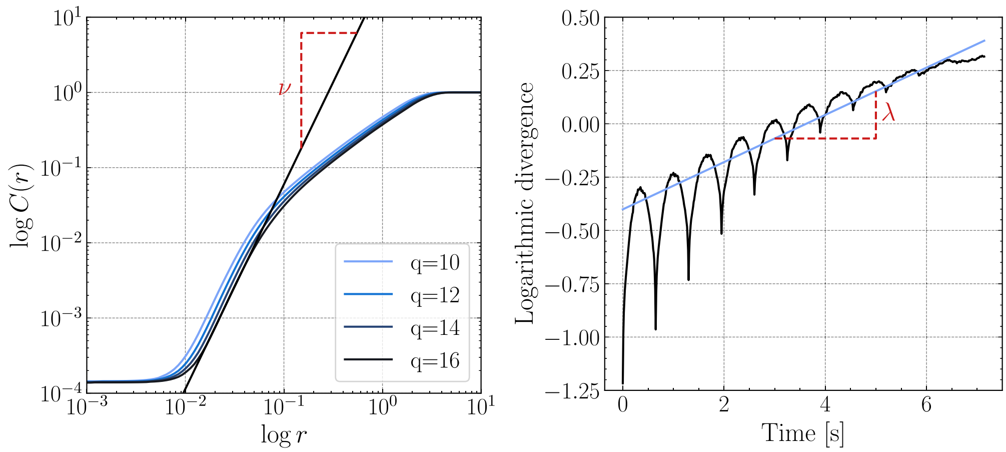

(a) (b)

Fig. 6. Identification of (a) the correlation dimension ν with the Grassberger and Procaccia algorithm and (b) the largest Lyapunov exponent λ_m with the Rosenstein algorithm. Both indicators were computed from a tensile test at a strain rate $\dot{\varepsilon} = 10^{-3}$ s^{-1}.

of band dynamics observed in stress–strain curves, and to identify transitions in their behaviour (Bharathi and Ananthakrishna, 2003; Lebyodkin and Estrin, 2005).

Multifractality provides a framework for characterising signals whose pointwise regularity varies significantly with time. This regularity is quantified using Hölder continuity, which defines the Hölder exponent h by comparing the local behaviour of the signal to a power-law. However, direct numerical estimation of the pointwise regularity at each location is often unstable. To address this difficulty, an alternative approach focuses on measuring the size of the set of points that share a given Hölder exponent. This size is typically quantified using the Hausdorff dimension D. The resulting function, which maps each exponent h to the Hausdorff dimension of its corresponding level set, defines the so-called multifractal spectrum (Jaffard et al., 2006):

$$D(h) = \dim_H \{t : h(t) = h\}. \quad (16)$$

As previously mentioned, computing the Hölder exponent pointwise is computationally intractable, especially for experimental signals. Consequently, several methods have been developed to estimate the multifractal spectrum from numerically computable quantities derived directly from the signal (Jaffard et al., 2006). These include approaches such as Multifractal Detrended Fluctuation Analysis (MF-DFA) (Kantelhardt et al., 2002), the box-counting method (Hentschel and Procaccia, 1983), and various wavelet-based techniques. Among the latter, the Wavelet Transform Modulus Maxima (WTMM) (Muzy et al., 1993) and the Wavelet Leaders method (WLMM) (Jaffard, 2004; Jaffard et al., 2006) are particularly prominent.

In this work, we adopt the WLMM for the computation of the multifractal spectrum. For brevity, we do not present the full theoretical background, as it is thoroughly covered in the literature (Jaffard, 2004; Jaffard et al., 2006; Wendt et al., 2007, 2009; Abry et al., 2012). Instead, we focus on the key components of the method and the relevant parameters that can be extracted from it.

The core of the WLMM — as with all multifractal analysis techniques
— lies in the computation of the structure function $S^L(q,\ell)$, where q denotes the moment order and ℓ a characteristic length scale. In the WLMM framework, this structure function is computed using *wavelet leaders*, which are defined as the maximum absolute value of wavelet coefficients within a local neighbourhood across scales and positions.

The structure function $S^L(q,\ell)$ characterises the scaling behaviour of the signal and is related to the *scaling exponent function* $\zeta(q)$ through the following power-law relation:

$$S^L(q,\ell) \sim \ell^{\zeta(q)}. \quad (17)$$

This relation captures the multiscale fluctuations of the signal.

Table 3
Summary of indicators used for PLC effect characterisation.

Indicator	Symbol	Indicator	Symbol
Serration amplitude[a]	$\Delta\sigma_n$	Power-law exponent[a]	b
Serration period[a]	$\Delta\varepsilon_n$	Correlation dimension[b]	ν
Serration amplitude power-law exponent[a]	η	LLE[b]	λ_m
Amplitude/period power-law exponent[a]	γ	Multifractal spectrum max cumulant[c]	c_1
Plastic activity power-law exponent[a]	a	Multifractal spectrum second cumulant[c]	c_2

[a] Statistical indicators.
[b] Dynamical indicators.
[c] Multifractal indicators.

In practice, direct computation of the singularity spectrum $D(h)$, which describes the distribution of Hölder exponents h, is not feasible. Instead, an upper bound known as the *Legendre spectrum* $L(h)$ is obtained via the Legendre transform of $\zeta(q)$:

$$D(h) \leq \inf_q (1 + qh - \zeta(q)) = L(h). \tag{18}$$

This transform is often found to be expressed as:

$$h(q) = \frac{\mathrm{d}\zeta(q)}{\mathrm{d}q}, \quad L(h) = qh - \zeta(q). \tag{19}$$

In experimental contexts, the Legendre spectrum $L(h)$ is commonly used as a proxy for the true multifractal spectrum $D(h)$. In fact, the two terms are often used interchangeably in the literature, and we adopt the same convention in the remainder of this text. The method introduced here can be extended to multidimensional signals, which allow for the characterisation of image textures by capturing their local irregularities and scale-invariant features (Wendt et al., 2009).

To quantitatively characterise the multifractal spectrum, we employ the *log-cumulant* introduced by Wendt et al. (2007). This approach relies on the Taylor expansion of the scaling function $\zeta(q)$ around $q = 0$, expressed as:

$$\zeta(q) = \sum_{p=1}^{\infty} c_p \frac{q^p}{p!}, \tag{20}$$

where the coefficients c_p are known as log-cumulants. In practice, only the first three log-cumulants — c_1, c_2, and c_3 — are typically estimated (Wendt et al., 2009), as they capture the key features of the multifractal spectrum. Specifically, c_1 corresponds to the position of the spectrum's maximum, c_2 reflects its width (i.e., the degree of multifractality), and c_3 quantifies the asymmetry of the spectrum. As such log-cumulants will be further used to characterise the multifractality of the signals studied along. In particular, the log-cumulants c_1 and c_2 provide the right framework to properly characterise some key features of the signal multifractal spectrum, such as the width of the signal, an appropriate indicator of the intermittency of the signal.

To analyse the time series, a suitable wavelet basis must be selected to perform the wavelet transform and construct the structure function. A scale range $2^{j_1} \leq 2^j \leq 2^{j_2}$ has to be selected over which the fitting is carried out. In the present study, we employ Daubechies wavelets. The number of vanishing moments of the wavelet basis and the range of scales are chosen to provide an appropriate balance between time and frequency localisation, and ensure a robust estimation, while minimising boundary effects and sensitivity to noise.

Finally, the list of the selected indicators and exponents is given in Table 3.

5. Results

The results of the statistical analysis fall into three main categories: characterisation of the impact of the machine-specimen stiffness, influence of the strain rate on overall curve statistics and spatio-temporal analysis of the plastic strain rate fields in the sample.

5.1. Influence of the machine stiffness on the PLC effect

The dynamics of the PLC effect is dependent of the experimental setup on which the tensile tests are performed. Two distinct dynamics emerge depending on whether the machine is soft or hard, meaning its stiffness is either negligible or infinitely high compared to that of the specimen (Penning, 1972; Kubin and Estrin, 1985; Cuddy and Leslie, 1972). To a first approximation, assuming small variations in gauge length and cross-sectional area, the behaviour of the machine can be described by the *machine equation*, which links the local strain rate to the prescribed load:

$$\frac{\dot{\sigma} S}{K L} + \frac{1}{L} \int_{(L)} \dot{\varepsilon}\, \mathrm{d}x = \dot{\varepsilon}_0 \tag{21}$$

where K is the machine–specimen stiffness, comprising the machine stiffness K_m and the specimen stiffness K_s, $\dot{\varepsilon}_0$ the macroscopically applied strain rate, S the cross-sectional area of the specimen and L its length. In the case of a soft machine, which also corresponds to stress controlled conditions as per Eq. (21), stress evolves with steps-like behaviour (Guillermin et al., 2023). Conversely, for a hard machine, which corresponds to strain rate controlled tensile tests, the behaviour is marked by the characteristic stress drops of the PLC effect.

To assess the influence of rigidity, the model introduced in Section 3 is used. The stiffness of the linear spring of Fig. 2 is varied in the range $K_m \in [10^2, 10^7]$ N mm^{-1}, and the simulations are performed at strain rates $\dot{\varepsilon} \in 10^{-4}, 10^{-3}, 10^{-2}$ s^{-1}. Results of the tensile test simulations are given in Fig. 7. From the simulations, we observe that the dynamical response of the PLC effect varies greatly with the machine's stiffness. For high stiffness, the usual behaviour is recovered, with type C, B and A serrations observed on the stress–strain curve. However, for a decreasing stiffness, periods of the serrations increase and the morphology of the serrations changes, up to recovering mixed serrations displaying a staircase-like behaviour typical of stress-controlled conditions. As such, by varying the stiffness, the model is able to capture the transition from a hard to a soft tensile testing machine. In particular, we show that the model successfully reproduces the experimentally observed behaviour reported by Tretyakov et al. (2021), where type A serrations transition to type C serrations as stiffness decreases.

To better understand this behaviour, we examine the effective strain rate measured during the tensile tests. It is obtained as the slope of a linear fit of engineering strain, computed with the virtual extensometer, as a function of time, once the specimen has entered the plastic regime. We observe in Fig. 8(a), that the measured strain rate is equal to the applied strain rate for stiffness higher than that of the specimen, identified at $K_s = 36691$ N mm^{-1}. However, at low stiffness, the measured strain rate drops, suggesting that the influence of the stress rate becomes dominant resulting in the mixed loading conditions.

For each simulation, serrations are detected and characterised using the procedure outlined in Section 4.1. Given the absence of noise in the simulation, no threshold is applied to filter the stress drops. In Fig. 8(b), the average amplitude follows two distinct trends. At low stiffness, it increases until reaching a maximum, after which it decreases with increasing stiffness, eventually stabilising at a plateau

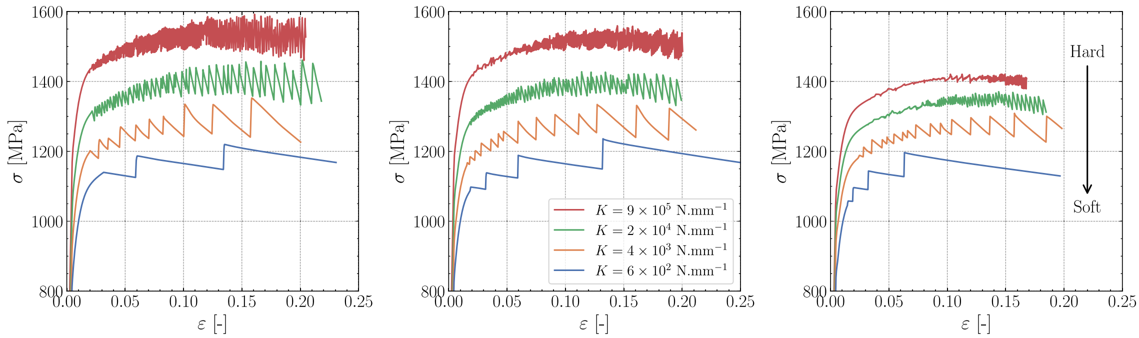

(a) $\dot{\varepsilon} = 10^{-4}$ s^{-1} (b) $\dot{\varepsilon} = 10^{-3}$ s^{-1} (c) $\dot{\varepsilon} = 10^{-2}$ s^{-1}

Fig. 7. Evolution of the stress–strain response as a function of machine stiffness for strain rates $\dot{\varepsilon} \in \{10^{-4}, 10^{-3}, 10^{-2}\}$ s^{-1}. Curves are vertically shifted for clarity. The transition from a hard to a soft machine regime induces a change in serration behaviour, with staircase-like patterns emerging at low stiffness, characteristic of stress-controlled conditions.

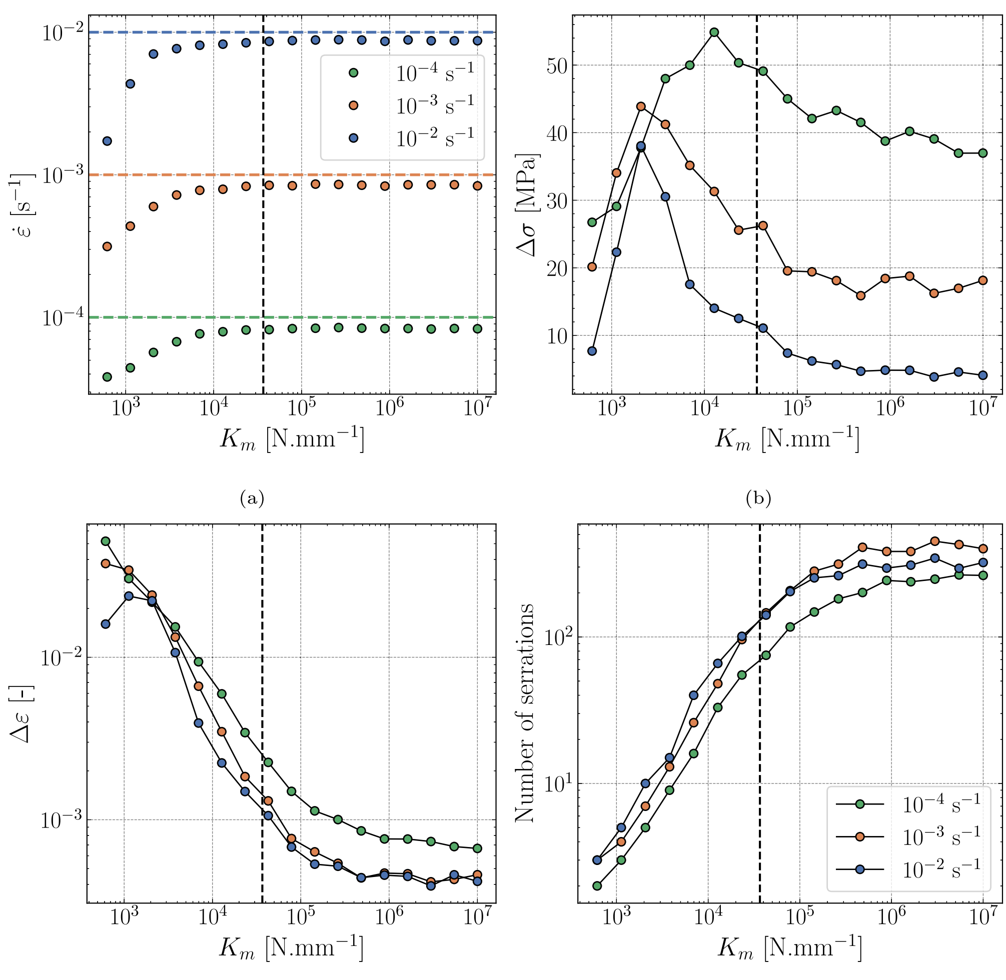

(a) (b) (c) (d)

Fig. 8. (a) Measured strain rate in function of the machine stiffness (b) Average amplitude of serrations in function of the machine stiffness (c) Average period of serrations in function of the machine stiffness (d) Number of serrations detected in function of machine stiffness. The vertical dashed line represents the specimen stiffness. We observe that all indicators stabilise once the machine stiffness is of several order of magnitude higher than the specimen stiffness. Plotted for strain rates $\dot{\varepsilon} \in \{10^{-4}, 10^{-3}, 10^{-2}\}$ s^{-1}.

when the machine stiffness is several orders of magnitude higher than that of the specimen. The behaviour of this indicator at low stiffness reflects the transition from a staircase-like stress response to the sharp stress drops characteristic of a stiff machine.

This trend is corroborated by the mean serration periods shown in Fig. 8(c) and the number of serrations in Fig. 8(d), which display an inverse relationship with respect to stiffness. As the number of detected serrations decreases, the strain interval between events increases, suggesting that the band carries a greater amount of strain. At low stiffness, serrations accommodate larger plastic strain increments, reducing the number of serrations required to fully plastify the specimen. This behaviour can be understood by examining Eq. (21). If we assume that plastic localisation occurs over a fraction f of the gauge length, and that the strain rate is uniform in this zone, the average strain rate is set to be equal to $f\dot{\varepsilon}_0$. It allows us to rewrite Eq. (21) as:

$$\dot{\sigma} = \frac{KL}{S}\,(1-f)\,\dot{\varepsilon}_0. \tag{22}$$

Thus, at low stiffness, when plastic strain rate localisation occurs, the stress rate is smaller. As a result, the stress drops become less abrupt, leading to the observed plateau, and the specimen undergoes more plastic deformation.

Our objective is to assess whether changes in stiffness affect the calculation of the correlation dimension and the Lyapunov exponent, as these indicators are central to characterising the PLC dynamics (Bharathi and Ananthakrishna, 2003). Specifically, they provide insight into the relationship between the macroscopic behaviour of the PLC effect and the finer dynamics occurring at smaller scales. Therefore, it is essential to determine whether these indicators remain unaffected by variations in machine stiffness.

An automatic time-stepping method is employed in the simulations to accurately capture localisation phenomena, so that the resulting strain–stress curves are non-uniformly sampled over time. This does not allow to use the algorithm described in Section 4, which assumes that the signal is sampled with a regular time step. Accordingly, signals were re-sampled, by interpolating stress–strain curves with splines and then sampling the interpolated function with a fixed time step. Then, serrations were extracted from the overall stress curve by using the stabilised model introduced in Section 3.2. The signal is then normalised by using the methodology in Section 4.1.

The evolution of the correlation dimension, shown in Fig. 9(a), reveals a consistent trend across all strain rates: it increases at low machine stiffness and stabilises once the stiffness is of several orders of magnitude larger than that of the specimen. This behaviour mirrors the transition previously observed in the statistical indicators, reflecting the shift from soft to hard machine regimes. This trend suggests a modification of the underlying serration dynamics, where reduced stiffness promotes a similar mode of band propagation across all strain rates. Furthermore, as shown in Video 2, the propagation evolves towards a front-type mode, in which the high plastic strain rate spans a large portion — if not the entirety — of the specimen gauge length. However, this apparent trend may also arise from the limited number of serrations observed at low stiffness, which can reduce the accuracy of the dimension estimation.

A similar pattern is observed for the LLE as shown in Fig. 9(b). At low stiffness levels, normalised LLE values fall within a comparable range, suggesting that serration dynamics remain similar under soft machine conditions, and is independent of strain rate. Conversely, in the hard machine regime, the LLE varies with strain rate, indicating that the deformation speed influences the nature of the serration dynamics.

These results demonstrate that the KEMC model consistently exhibits chaotic behaviour, as evidenced by the fractal nature of the attractor and the persistence of positive LLEs across all machine stiffness levels. This suggests that the onset of chaos is intrinsic to the model and not dependent on the specific experimental setup. However, the clear variation of these indicators with stiffness points to the existence of two distinct dynamical regimes, linked to the emergence of staircase-like behaviour under soft machine conditions.

The practical implications of these findings are substantial for both experimental and modelling approaches to the PLC effect. The proposed finite element model accurately captures the variations in PLC dynamics induced by changes in machine stiffness, as demonstrated experimentally by Tretyakov et al. (2021). Notably, statistical and dynamical indicators exhibit significant variability at low machine stiffness but stabilise once the machine stiffness significantly exceeds the specimen stiffness. Therefore, accounting for machine stiffness is crucial when setting up finite element simulations. As such, careful consideration of the tensile machine and test specimen design is necessary to minimise the influence of machine stiffness, in particular to perform comparison across various materials and experimental setups.

5.2. Influence of strain rate on the PLC effect

To evaluate whether the KEMC model can capture the wide diversity of behaviour observed experimentally, 45 simulations were performed in the strain rate range $[10^{-5}, 10^{-1}]$ s^{-1} and compared to the experimental results given in Section 2.2. Statistical and dynamical indicators were then used to characterise the dynamics displayed in simulations and experiments, using the methodology described in Sections 4 and 5.1.

It was demonstrated in Section 5.1 that accounting for machine stiffness in the modelling is essential, as it significantly affects the dynamics and characterisation of serrations. To determine the setup stiffness, simulations were performed on the flat specimen geometry assuming purely elastic behaviour. The resulting force–displacement curves were then compared to the experimental data, yielding a specimen stiffness of $K_s = 36691$ N mm^{-1}. This value is subsequently used in all following simulations.

5.2.1. Statistical analysis

The values of the statistical indicators are compiled in Fig. 10. Within the strain rate range $[10^{-5}, 10^{-2}]$ s^{-1}, type B and C serrations are observed in both simulations and experiments. Amplitudes (Fig. 10(a)) and periods (Fig. 10(b)) decrease with increasing plastic strain rate. Moreover, as each serration carries lower amount of plastic strain, the number of recorded events increases, as shown in Fig. 10(c). This trend is consistent with the physical mechanisms of DSA, where smaller deformation rates allow more dislocations to get pinned and more solutes to diffuse towards them, leading to more intense serrations upon unpinning.

Serration amplitudes follow a power-law dependence, $\Delta\sigma \propto \dot{\varepsilon}^{-\eta}$. An exponent of $\eta^{\mathrm{BC}}_{\mathrm{simu}} = 0.24$ is obtained from the simulations, closely matching the experimental value of $\eta^{\mathrm{BC}}_{\mathrm{exp}} = 0.21$. Furthermore, the average plastic strain carried by the bands during serrations is found to be of the same order of magnitude in both experiments and simulations. These results indicate that, within this range of strain rates, the model effectively captures the dynamics of the PLC effect as reflected in key statistical measures.

Beyond the threshold value of $\dot{\varepsilon} = 10^{-2}$ s^{-1}, the average periods and the number of serrations reach an extremum, after which they increase and decrease with strain rate, respectively. While the average amplitudes continue to decrease, they do so at a significantly faster rate, marked by a change in slope and characterised by an exponent of $\eta^{A}_{\mathrm{simu}} = 1.12$. This shift in the dynamics of the simulated PLC effect is associated with a transition from type CB to type A bands.

At such high strain rates, plastic relaxation becomes limited, as the stress remains near the critical value required to trigger a plastic burst. Physically, this corresponds to a regime in which solute atoms do not have sufficient time to fully segregate towards the pinned dislocations, thereby exerting only a partial influence on their dynamics. As a result, the serration amplitudes decrease and the number of recorded events declines, as a single, continuously propagating band replaces the repeated yield drops characteristic of type B and C serrations.

The significant discrepancy between experiments and simulations observed at $\dot{\varepsilon} = 10^{-1}$ s^{-1} in Fig. 10(b) can be attributed not only to a transition in serration behaviour but also to reduced measurement

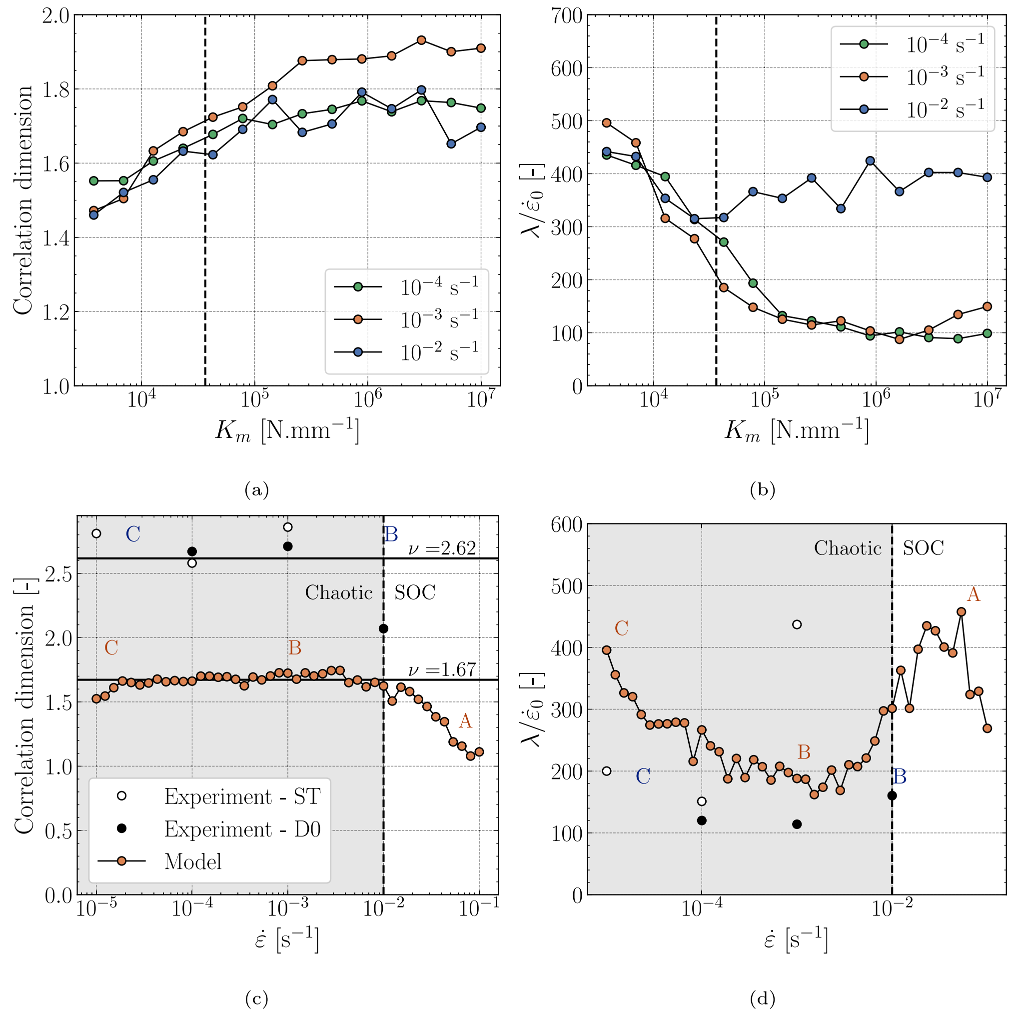

Fig. 9. Evolution of the correlation dimension (a, c) and the normalised largest Lyapunov exponent, $\lambda/\dot{\varepsilon}_0$, (b, d) as functions of machine stiffness (a, b) and strain rate (c, d). Both indicators reach a plateau once the machine stiffness exceeds the specimen stiffness — indicated by the dotted line — by several orders of magnitude. At low machine stiffness, similar LLE values indicate that soft-machine conditions lead to comparable dynamics regardless of other parameters. For a given stiffness, K_s = 36691 N mm^{-1}, the correlation dimension remains constant during type B and C serrations but decreases at high strain rates, signalling the transition to type A bands and marking a shift from chaotic to SOC dynamics. The chaotic domain obtained from simulations is shown by the grey-shaded area. Lower correlation dimensions in simulations compared to experiments indicate that the simulated PLC effect evolves within a reduced phase space. The evolution of the normalised LLE in simulations follows the same trend observed experimentally. The corresponding band types are indicated in red and blue for simulations and experiments, respectively. (For interpretation of the references to colour in this figure legend, the reader is referred to the web version of this article.)

accuracy at high tensile testing speeds, which tend to overestimate strain values.

While a transition from type B to type A bands is predicted by the simulations, it is not observed experimentally, as type B bands persist at high strain rates. However, a similar transition in serration dynamics has been reported in Al-Mg alloys by Klose et al. (2004) (see figure 8 in the latter reference). In that study, the exponents associated with type B and C serrations range from $\eta^{BC} \in [0.18, 0.28]$, which aligns well with our findings. For type A serrations, reported exponents fall within $\eta^{A} \in [0.54, 0.89]$, indicating a steeper decrease of serration amplitudes – a behaviour that is accurately reproduced by the model.

These results suggest that for two different alloys, the evolution of serration amplitudes as a function of strain rate consistently follows a power-law relationship. Notably, the exponents obtained for type B and C bands are of the same order of magnitude regardless of the material.

As shown in Fig. 11, a correlation between mean amplitudes and periods is observed in both experiments and simulations, following a power-law relationship $\Delta\varepsilon \sim \Delta\sigma^{\gamma}$ within the strain rate range $\dot{\varepsilon} \in [10^{-5}, 10^{-2}]$ s^{-1}. For higher strain rates a plateau is reached. This pattern is exclusively associated with type B and C serrations. The experimental exponent is found to be $\gamma_{exp} = 0.91$, while the simulation yields $\gamma_{sim} = 0.92$, indicating a strong agreement. The presence of this relationship in both cases, along with the similarity of the exponents, suggests that the KEMC model effectively captures the key dynamics of type B and C serrations.

5.2.2. Dynamical analysis: from chaos to SOC

Analysing serration properties alone is insufficient to validate the reliability of the model, as accurately replicating serration timing and characteristics remains challenging. As outlined in Section 4, dynamical systems' theory provides a comprehensive framework for quantifying signal dynamics and comparing simulation results to experimental data. To gain qualitative insights into the dynamics of the PLC effect, the attractor has been reconstructed following the method of Section 4.2. For a tensile test at a strain rate $\dot{\varepsilon} = 10^{-3}$ s^{-1}, the experimental attractor is shown in Fig. 5(a) and the simulated one in Fig. 5(b). The

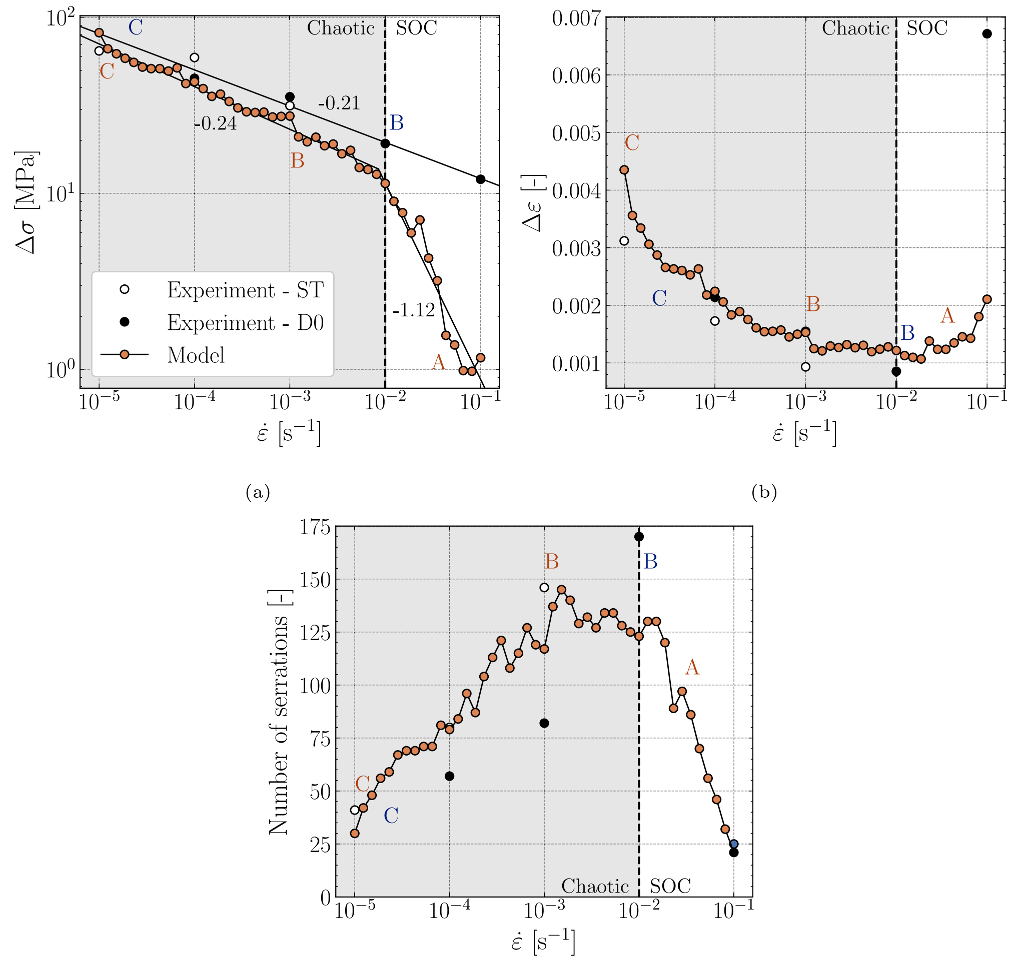

(c)

Fig. 10. Average amplitudes (a), average periods (b), and number (c) of serrations in function of the strain rate. The experimental trends are reproduced by the simulations except at high strain rates. The amplitudes are correlated to strain rate through a power law $\Delta\sigma \sim \dot{\varepsilon}^{-\eta}$, dependent on the band dynamics: $\eta_{exp} = 0.21$, $\eta_{sim}^{BC} = 0.24$, $\eta_{sim}^{A} = 1.12$. Maximum number of serrations is observed for type B serrations where hoping bands are found. Corresponding band types are indicated in red and blue for simulation and experiments, respectively. The chaotic domain obtained from simulations is shown by the grey-shaded area. (For interpretation of the references to colour in this figure legend, the reader is referred to the web version of this article.)

two attractors exhibit strikingly similar dynamics, characterised by a straight line corresponding to the reloading phase of the tensile curve and a swirling flow representing the onset of a serration.

From the reconstructed attractors, the correlation dimension and the Lyapunov exponents are then computed. In Fig. 9(c), the correlation dimension remains approximately constant for type B and C serrations, with a mean value of $\nu_{simu} = 1.75$. However, upon reaching a strain rate of $\dot{\varepsilon} = 10^{-2}$ s^{-1}, the computed dimension decreases, indicating, again, the emergence of type A serrations. At the highest strain rates, the value of the dimension is found to be close to 1 suggesting that the attractor does not display fractal properties.

The evolution of the LLE is shown in Fig. 9(d). We first observe that the indicators computed from both simulations and experiments are of the same order of magnitude. Similar to the correlation dimension, the LLE captures the transition in serration dynamics through two distinct features. Starting from low strain rates, increasing the strain rate leads to a decrease in the LLE, reflecting the transition from type C to type B bands. Upon further increasing the strain rate, the LLE rises again, indicating the transition from type B to type A bands. This evolution is consistent with the period variations shown in Fig. 10(b). In this case the increase in the LLE values at high strain rates are thus associated with larger strain increments, even though the underlying mechanisms behind this behaviour may differ between type C and type A serrations.

From these results, it can be concluded that, within the domain of type B and type C serrations, non-integer correlation dimensions and positive LLE values are observed, further suggesting that these peculiar modes of band propagation are associated with chaotic dynamics. Although a positive LLE is also observed at high strain rates, the concurrent decrease in the correlation dimension towards values close to 1 prevents us from asserting the presence of chaotic behaviour in this regime. Experimentally, this shift in dynamics has been associated with the emergence of self-organised criticality (SOC) (Bharathi and Ananthakrishna, 2003; Bharathi et al., 2002; Lebyodkin et al., 1995), which is typically linked to type A band dynamics. However, in our case, we observe an increase in the largest LLE, contrary to the expected trend where it would converge towards zero, as is typical for systems exhibiting SOC dynamics (Chen et al., 1990).

SOC refers to systems that spontaneously evolve towards a critical state, exhibiting scale-invariant dynamics characterised by avalanche-like behaviour and long-range correlations. In the context of the PLC effect, SOC manifests a power-law distribution of serration amplitudes and periods. Specifically, the probability density function (PDF) of a variable of interest x follows a power law, $p(x) \sim x^{-b}$, where b is the

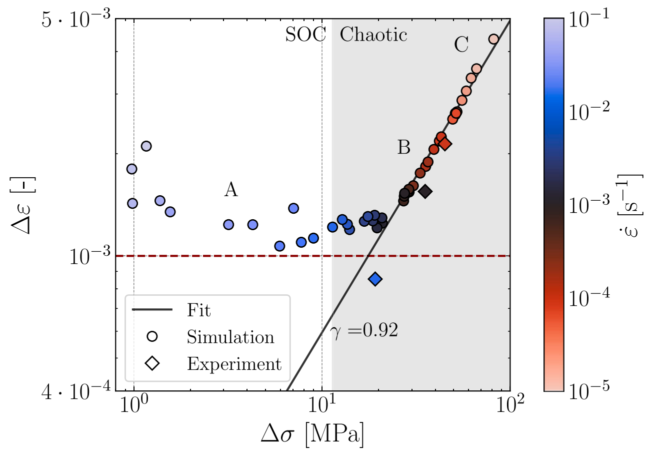

Fig. 11. Serrations average strain increments in function of the average stress drops reported during a tensile experiment or simulation. Simulations are represented by circle markers while experiments are represented by diamond markers. Corresponding simulated regimes are indicated on the curve. Power law relations, $\Delta\sigma \sim \Delta\varepsilon^{-\gamma}$, are found for type B and C dynamics, where $\gamma_{exp} = 0.91$, $\gamma_{sim} = 0.92$. A plateau is observed at the emergence of type A serrations. At low strain rates a plateau is reached in the simulations, indicated by the red dotted line. The chaotic domain obtained from simulations is shown by the grey-shaded area. (For interpretation of the references to colour in this figure legend, the reader is referred to the web version of this article.)

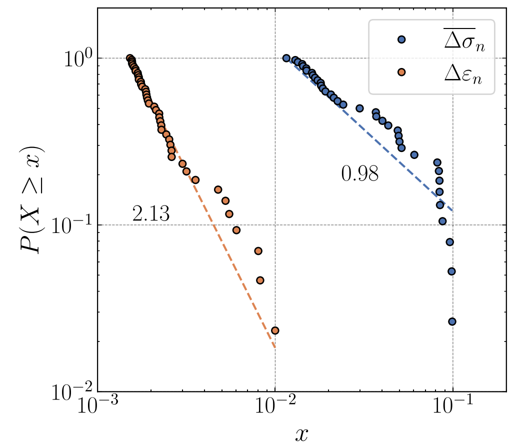

Fig. 12. Complementary Cumulative Distribution Function (CCDF) plot of strain increments and normalised stress drop amplitudes at a strain rate $\dot\varepsilon = \times 10^{-2}$ s^{-1}. x is either representative of $\overline{\Delta\sigma}$ or $\Delta\varepsilon$. Power law distribution is observed for both indicators. The CCDF exponent is related to the PDF exponent as $b_{CCDF} = b - 1$ which yields $b_{\overline{\Delta\sigma}} = 1.98$ and $b_{\Delta\varepsilon} = 3.13$.

critical exponent of the distribution. For practical identification from experimental data, one often considers the complementary cumulative distribution function (CCDF), defined as the complement of the cumulative probability: $\mathrm{CCDF}(x) = 1 - \int_{x_{\min}}^{x} p(x')\,dx' \sim 1 - x^{-(b-1)}/(b-1)$ for $x \gg x_{\min}$. An example of such power-law behaviour is illustrated in Fig. 12 for a strain rate of $\dot\varepsilon = 10^{-2}$ s^{-1}, where both the serration amplitude and period exhibit power-law scaling. This behaviour is consistently observed for all strain rates above this threshold, with average critical exponents measured as $b_{\overline{\Delta\sigma}} = 1.70$ and $b_{\Delta\varepsilon} = 2.69$. The power-law scaling of stress drops is in agreement with previous observations in the literature (Bharathi et al., 2001, 2002). In contrast, one would generally expect the distribution of serration periods to follow a Poisson law, as reported for waiting times between successive serrations (Lebyodkin et al., 2017). Nevertheless, the exponent measured for the stress drop distribution in our simulations is close to that reported for AlMg alloys by Bharathi et al. (2001), where $b_{\overline{\Delta\sigma}} = 1.5$.

The transition from type B to type A bands is well captured by the finite element model and is associated with a power-law distribution of serrations amplitudes and periods, suggesting that the model is able to simulate the SOC dynamics in this specific case. This result is found to be consistent with experimental observations found in the literature (Bharathi et al., 2002). This transition is marked by a decrease in the correlation dimension, indicating the coexistence of mixed-mode dynamics during the tensile tests, with SOC behaviour being recorded at the early stages of the experiments, slowly evolving towards a chaotic response at higher strains. This transition is also well captured by the inflection of the normalised LLE at high strain rates, indicating a shift towards SOC dynamics.

From an experimental standpoint, the correlation dimension for type B and C serrations remains constant, as shown in Fig. 10(a), with an average value of $\nu_{\mathrm{exp}} = 2.62$. The Lyapunov exponents show similar behaviour in both experiments and simulations, indicating chaotic dynamics and supporting the relevance of the model. However, the highest correlation dimension observed in the experiments suggests that the reconstructed attractor exists in a phase space with greater dimensionality than that of the simulations. This discrepancy implies that the model captures less complex dynamics compared to the experimental observations.

5.2.3. Multifractal analysis

Multifractal analysis is performed across all strain rates for both simulated and experimental datasets. Daubechies wavelets of order $N_\psi = 4$ is used for each case. The multifractal properties are obtained by performing a weighted fit over the scales $j_1 = 3$ and $j_2 = 10$. The indicators c_1 and c_2, which represent the position and width of the spectrum maximum as described in Section 4, are computed from the resulting multifractal spectrum. The results are presented in Fig. 13 for both experiments and simulations.

Initially, we observe that the position of the maximum and the width of the spectrum are significantly overestimated in the simulations compared to the experimental results. This discrepancy can be attributed to the differences between the experimental and simulation datasets. In the simulations, discrete microplastic events and noise are absent, whereas they are present and discernible in the experimental data. As a result, finer-scale dynamics is not captured in the simulations, leading to the predominance of strongly discontinuous events in the multifractal spectrum, which in turn increases its width.

To better understand the impact of noise and finer-scale events, we model them as Brownian noise, with time increment $\Delta t = 10^{-7}$ s and scaled as an hundredth of the difference between minimum and maximum recorded in the signal. The noise is then added to the normalised stress curve. As shown in Fig. 13, the introduction of noise significantly reduces the magnitudes of both cumulants. In particular, c_2 now falls within the same order of magnitude as observed in the experiments. This suggests that the noise compensates for the dominance of serrations in the multifractal spectrum calculations. Thus, the spectrum can be interpreted as a combination of global dynamics — represented by the serration dynamics — and finer-scale dynamics, captured by the noise, which also accounts for smaller plastic events that do not appear in the simulated tensile curves.

Even if the finer scales are not taken into account in the modelling, some trends are observable from the computations of the multifractal indicators, in the simulation. The first cumulant c_1 which describes the position of the maximum of the multifractal spectrum, decreases with strain rate, as observed in the simulations. The second cumulant, c_2, which determines the width of the spectrum, peaks at a strain rate which corresponds to type B bands dynamic. Therefore, at this strain rate, the maximum irregularity in the signal is reached. This

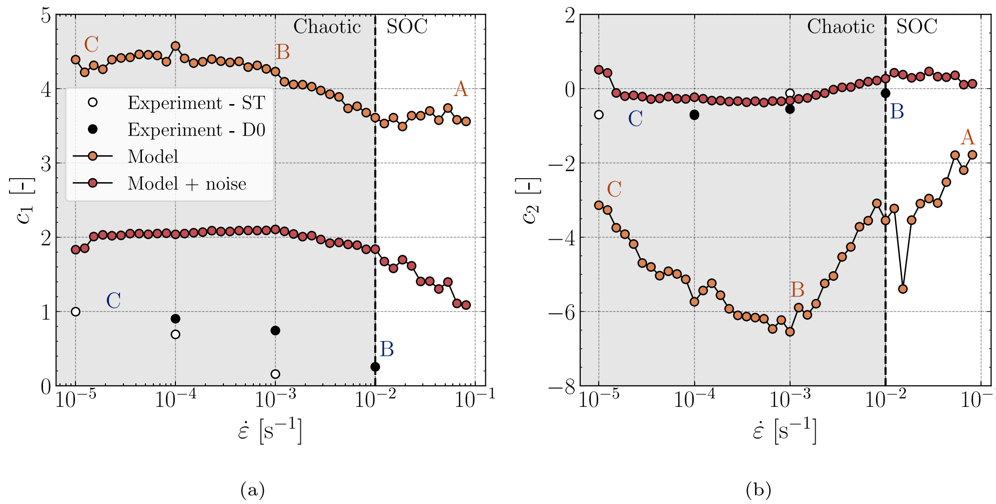

Fig. 13. Evolution of (a) the first cumulant, c_1, and (b) the second cumulant, c_2 in function of the strain rate. The cumulants computed from the simulations are larger than those measured from the experiments. This is mitigated by introducing noise into the signal. Decrease of c_1 is associated to the emergence of type A serrations while the minimum of c_2 is observed for type B serrations. Corresponding band types are indicated in red and blue for simulation and experiments, respectively. The chaotic domain obtained from simulations is shown by the grey-shaded area. (For interpretation of the references to colour in this figure legend, the reader is referred to the web version of this article.)

result suggests that multifractal analysis can be used to classify the type of bands observed during a tensile test, as previously suggested by Bharathi and Ananthakrishna (2003). In particular, the simulation results highlight the capability of this method to detect transition from type C to type B serrations and then from type B to type A serrations.

5.3. Spatio-temporal dynamics of the PLC effect

The dynamics of the PLC serrations are closely related to the propagation modes of the plastic strain rate localisation bands within the tensile specimen. A practical approach to visualise the propagation of the bands is to use spatio-temporal diagrams of the normalised plastic strain rate $\dot{p}/\dot{\varepsilon}_0$ (Valmalle et al., 2024), as they provide a condensed overview of serrations dynamics during a tensile test. Diagrams are constructed by recording the evolution of the strain rate along a line spanning the gauge length at each time step, displayed by the red line in Fig. 2.

The spatio-temporal diagrams shown in Fig. 14 exhibit the characteristic zebra-like patterns associated with different PLC band propagation modes (Mazière et al., 2010a). To facilitate a detailed comparison between localisation behaviour and serration dynamics, each diagram is paired with its corresponding stress–strain curve, from which the general strain hardening has been subtracted to enhance the visibility of serrations. Two representations are provided: one with overall strain on the x-axis and another with time, offering complementary views of the spatio-temporal evolution. In both cases, the horizontal white lines mark the boundaries of the gauge length. Spatio-temporal diagrams were generated at three different strain rates—10^{-5}, 10^{-3}, and 10^{-2} s^{-1}.

On these diagrams, type C,B and A serrations are distinctively observed with their associated spatial propagation mode (Rodriguez, 1984). For type B and C bands (Figs. 14(b) and 14(d)), each stress drop corresponds to a temporally localised plastic event. When visualised against strain (Figs. 14(a) and 14(c)), these events appear more extended, revealing the significant plastic deformation occurring during the stress drop. The plastic activity in time-based diagrams primarily represents residual plastic strain rates during elastic reloading phases following stress drops.

Type A serrations (Figs. 14(e) and 14(f)) exhibit less temporally localised plastic activity. This behaviour characterises high strain rates, where smaller timescales do not allow for complete plastic relaxation during stress drops. Consequently, the strain rate within bands is of the same order of magnitude as the applied rate, resulting in continuous propagation rather than discrete plastic bursts. In this regime, the most significant stress drops typically coincide with the interaction of propagating bands with the specimen's fillets.

As shown in Fig. 14, the PLC dynamics display significant heterogeneity across all strain rates, with simultaneous high and low plastic activity zones along the gauge. To analyse these distributions, we studied the spatio-temporal diagram within a confined zone inside the gauge length, as depicted by the two white plain horizontal lines, from the first serration to the Considère criterion. To quantify a signal comparable to experimental measurements, we constructed a diagram with time as the x-axis, similar to what would be obtained from Digital Image Correlation. The simulation data featured irregular time-steps that could not be used directly. We then re-sampled the signal by first interpolating the curve with first-order splines and then sampling the interpolated function with a fixed time-step. The resulting images had a resolution of 64 × 8092 pixels.

The distribution of plastic strain rate events normalised by the applied strain, recorded in the area of interest, is presented in Fig. 15. It confirms the earlier observation that the most intense events — responsible for most of the plastic deformation — occur less frequently than lower-amplitude events, which are more diffusely scattered across the diagram. Quantitatively, the plastic activity follows a power-law distribution, $\sim (\dot{p}/\dot{\varepsilon})^{-a}$. The critical exponents associated with type C, B, and A bands are $a_C = 1.17$, $a_B = 1.23$, and $a_A = 1.18$, respectively. This power-law behaviour indicates that plastic deformation exhibits scale-invariant features. Notably, the consistency of the exponent values across all band types ($a \approx 1.2$) suggests that the spatial distribution of plasticity is statistically similar, independently of the mode of localisation of the PLC plastic strain rate bands.

To quantify the heterogeneity of the spatio-temporal dynamics observed in the diagrams, multifractal analysis is employed and extended to multidimensional signals. The analysis is conducted on the same images previously used for the statistical study of plastic activity. Daubechies wavelets with $N_\psi = 3$ vanishing moments are used, and the multifractal attributes are derived from weighted fits performed over the scales $j_1 = 3$ to $j_2 = 6$.

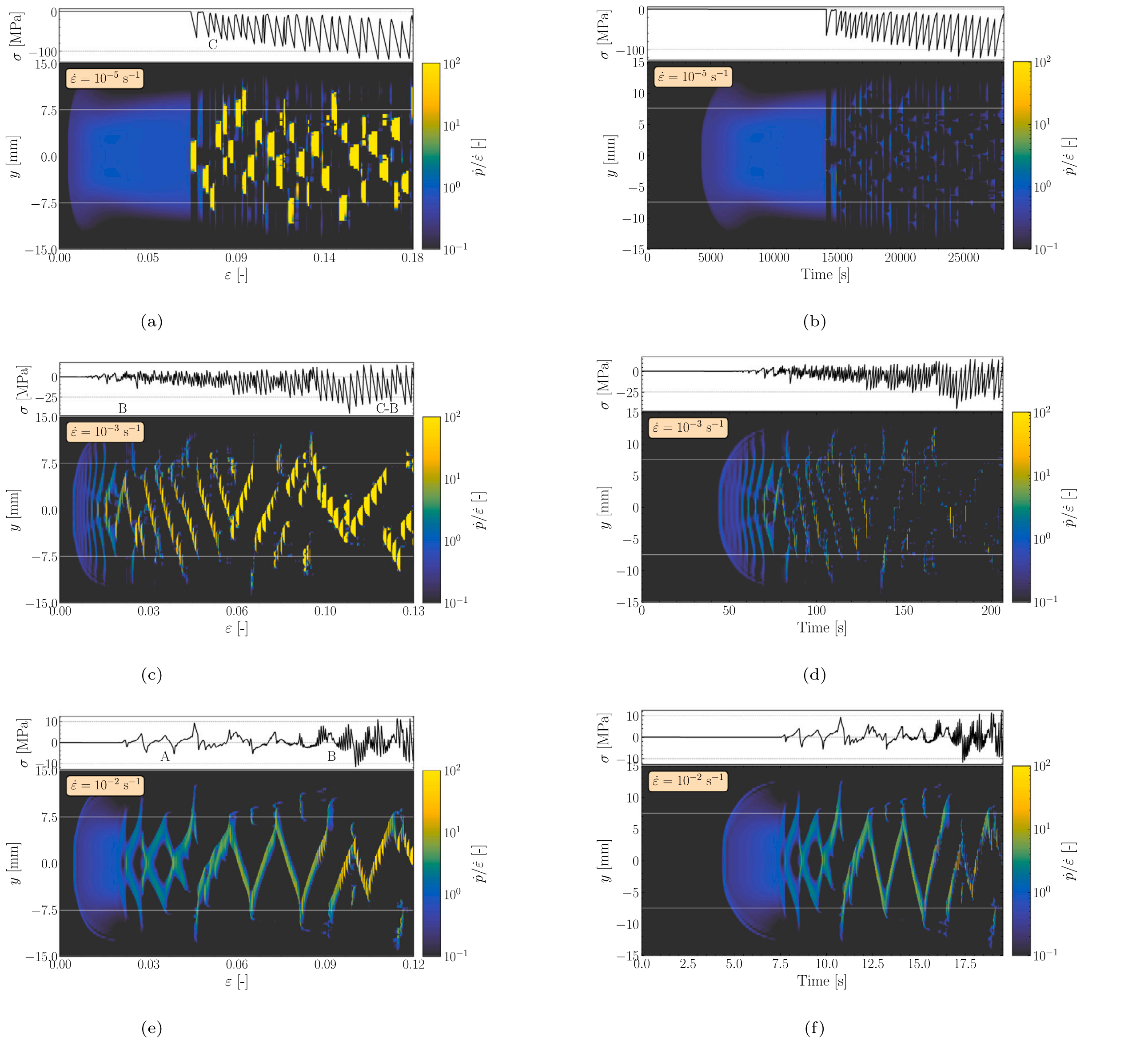

Fig. 14. Simulated spatio-temporal diagrams of the PLC effect for strain rates $\dot{\varepsilon} \in \left\{10^{-5}, 10^{-3}, 10^{-2}\right\}$ s^{-1}, including the companion stress/strain diagrams, from which general hardening has been removed. Horizontal lines in white indicate the boundaries of the gauge length. (a–c–e) Strain dependent diagrams. (b–d–f) Time dependent diagram. We observe that time dependent diagrams do not allow one to visualise the whole magnitude of the localisation. The propagation modes are visualised with randomly, hoping and continuously propagating bands corresponding to type C, B and A type bands. Each localisation is associated to a stress drop. For type A band, major stress drops are associated to the interaction with the fillet of the specimen.

The resulting multifractal spectra for each strain rate are shown in Fig. 16. The width of the multifractal spectrum increases as the strain rate decreases. This indicates a greater heterogeneity of plastic strain rate localisation at lower strain rates. The observed behaviour aligns with the known dynamics of PLC bands. At low strain rates, type C bands dominate, characterised by intermittent, localised plastic events scattered irregularly across the specimen. These dynamics lead to a broader multifractal spectrum. In contrast, at high strain rates, type A bands — marked by continuously propagating deformation — produce a more spatially and temporally uniform response, resulting in a narrower spectrum with fewer strong singularities.

It is therefore emphasised that multifractal analysis represents a powerful methodology for the examination of spatio-temporal diagrams of the PLC effect. This technique enables the quantification of signal heterogeneity and texture, which decreases with strain rate, thereby facilitating the classification of the various localisation modes.

6. Discussion

6.1. Characterisation of the dynamics of the PLC effect

The multifaceted analysis of the PLC effect reveals intricate relationships between statistical, dynamical, and multifractal indicators, offering a comprehensive characterisation of its underlying dynamics. As discussed in Section 5.2, serration behaviour is closely linked to band propagation types and is consistently captured by these indicators. Their variations reflect a transition from chaotic to SOC dynamics at high strain rates, corresponding to the shift from type CB to type A bands.

Two distinct groups of correlated indicators emerge from this analysis. The first group consistently detects the B-to-A serration transition through characteristic shifts at approximately $\dot{\varepsilon} \simeq 10^{-2}$ s^{-1}. Serration

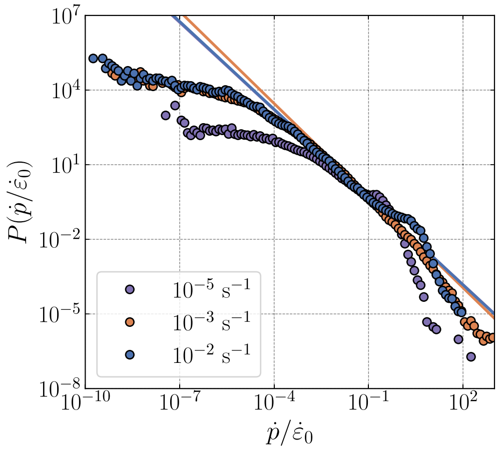

Fig. 15. Probability distribution function of plastic strain rate recorded along the tensile specimen gauge zone for strain rates of 10^{-5}, 10^{-3}, and 10^{-2} s^{-1} during simulations. The plastic strain rate is normalised by the macroscopically applied strain rate in order to allow for comparison. The simulations data follow power law distributions $(\dot{p}/\dot{\varepsilon})^{-a}$ with similar exponents for all strain rates where $a_C = 1.17$, $a_B = 1.23$, and $a_A = 1.18$ for type C, B, and A serrations, respectively.

amplitudes (Fig. 10(a)) exhibit a slope change, while serration periods (Fig. 10(b)) reach a minimum before increasing with strain rate. This combined evolution disrupts the power-law relationship between amplitudes and periods, as shown in Fig. 11. Similarly, the correlation dimension (Fig. 9(c)) remains constant for type B and C serrations but decreases upon type A band formation.

The second group of indicators — including the LLE (Fig. 9(d)), multifractal spectrum width (characterised by log-cumulant c_2), and serration count (Fig. 10(c)) — follows different trends, all reaching extrema at $\dot{\varepsilon} \simeq 10^{-3}$ s^{-1}, corresponding to the type B band regime.

These consistent trends across fundamentally different indicator types highlight their sensitivity to the spatio-temporal characteristics of band propagation (Fig. 14). Despite their distinct construction methodologies, all indicators capture similar underlying transitions in system behaviour. Consequently, each serves as a valid proxy for identifying and distinguishing between PLC dynamic modes, with the choice depending on specific analytical objectives and the complementary insights desired.

6.2. Insights on type a bands serrations dynamics

As discussed in Section 5.3, the dynamics of serrations—particularly for type A bands is influenced by interactions between plastic strain rate bands and the specimen geometry. In these cases, significant stress drops occur when propagating bands diffuse or reflect at the specimen's fillets.

To further examine the specific dynamics of type A bands, a simulation was conducted at a strain rate of $\dot{\varepsilon} = 10^{-2}$ s^{-1} on a plate geometry representative of the gauge zone of the flat specimen, with dimensions 10×15×2 mm. A spatio-temporal diagram was constructed from this simulation to visualise the propagation behaviour and temporal evolution of the plastic localisation bands. In this finite element model, type A bands exhibit continuous propagation of plastic localisation across the specimen, as shown in Fig. 17(a). Notably, a distinct reflection pattern emerges, where bands bounce back and forth between the specimen ends—producing a *ping-pong* propagation mode reminiscent of a wave reflecting within a confined domain. Each interaction of the band with the specimen boundary is marked by a white line in the spatio-temporal diagram and corresponds to a stress drop in the stress–strain response. This reflection-driven behaviour contrasts with the serration dynamics observed at lower strain rates, such as for type B and C bands, where sharp stress drops are typically associated with the sudden nucleation of localised plastic events within the gauge region.

Building on the previous analysis of type A band dynamics, an additional simulation was carried out to assess the influence of specimen length on band propagation at the same strain rate. The results for a longer plate of dimensions $10 \times 37.5 \times 2$ mm are shown in Fig. 17(b). Compared to the shorter specimen, we observe that the strain intervals between successive stress drops caused by band reflections increase, as the bands must now travel a greater distance to plastify the gauge. In addition to these reflection-related events, other stress drops are visible, corresponding to sudden changes in the band's trajectory or its relocation to a different position within the specimen. These stress drops occur without clearly identifiable plastic bursts, in a marked contrast with type B and C serrations.

These results underscore the distinctive nature of type A band dynamics, where stress drops are governed less by localised plastic bursts and more by the continuous propagation and interactions of the bands with specimen boundaries. Such mechanisms are also prevalent in the full specimen simulations, as illustrated in Fig. 14(e). In the dog-bone specimen, both propagation and boundary-induced reflection phenomena occur concurrently and display features similar to that of the plate. In a particular case, a sharp stress drop is observed when the propagating band reaches one end of the specimen and subsequently relocates to the opposite side, combining the two mentioned effects simultaneously.

The emergence of type A bands is linked to the reduced ageing time available following the passage of a band, as discussed in Section 6.3. To accommodate the imposed displacement rate, the material must nucleate plastic localisation bands more frequently. This increase in nucleation rate leads to smaller serration amplitudes and promotes continuous band propagation, resulting in the sharp decline in average amplitudes shown in Fig. 10(a).

At high strain rates, large-amplitude events — primarily driven by interactions between bands and the specimen's geometry — become increasingly rare. This scarcity contributes to the emergence of power-law distributions in both the periods and amplitudes of serrations, and to the observed rise in average period with increasing strain rate.

6.3. Phase space of the KEMC model

The characterisation tools introduced in Section 4 allow for the reconstruction of the PLC attractor from the stress time series. This attractor was subsequently used to compute the correlation dimension and Lyapunov exponents which serve as criteria to identify the chaotic behaviour of the PLC effect. According to Taken's theorem (Takens, 1981), the reconstructed attractor evolves in an equivalent phase space, that retains similar geometric and dynamic characteristics. This methodology offers valuable insight into the phase space of the KEMC model and the behaviour of its governing equations during finite element simulations.

In the KEMC set of equations, the internal variables responsible for the serrated dynamics is the ageing time t_a and the plastic strain rate $\dot{p}$. They evolve according to the relaxation equation Eq. (8) and the viscoplastic flow rule Eq. (5), respectively. Their coupled evolution is depicted in Fig. 18, based on data from Gauss points located at the center of the gauge section, within the plastic strain interval $p \in [0.11, 0.12]$, for strain rates $\dot{\varepsilon} = 10^{-5}$ s^{-1} and $\dot{\varepsilon} = 10^{-2}$ s^{-1} in Figs. 18(a) and 18(b). To facilitate the interpretation of the phase space dynamics, a schematic representation of the two resulting attractors is provided in Fig. 18(c), for $\dot{\varepsilon} = 10^{-5}$ s^{-1}. The corresponding stress evolution over the same plastic strain interval is shown as a function of time in Fig.

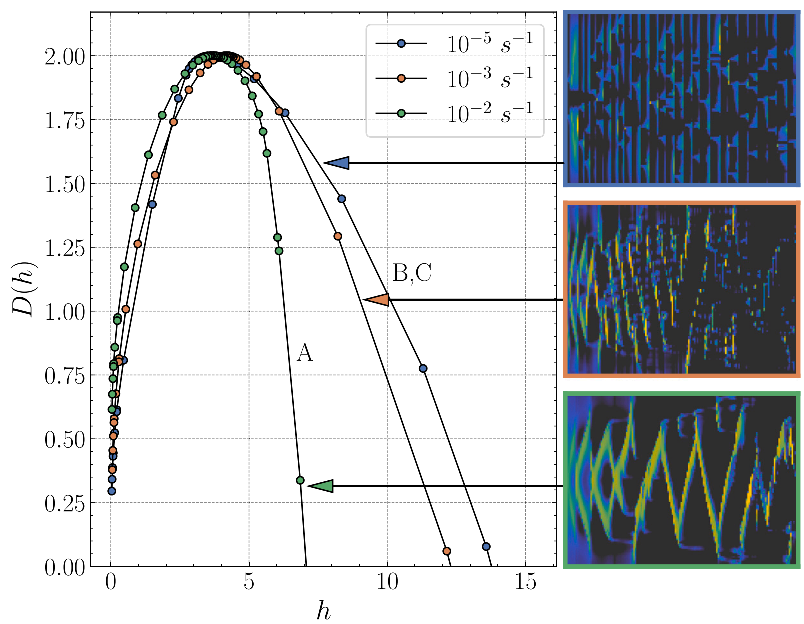

Fig. 16. Multifractal spectrum of the simulated spatio-temporal diagrams, depicted in the insets, for strain rates of $\dot{\varepsilon} \in \{10^{-5}, 10^{-3}, 10^{-2}\}$ s^{-1}. The spatio-temporal diagrams used for the computation are given and related to their corresponding spectrum. It is found that the width of the spectrum decreases with the strain rate, describing the transition from CB to A band-types.

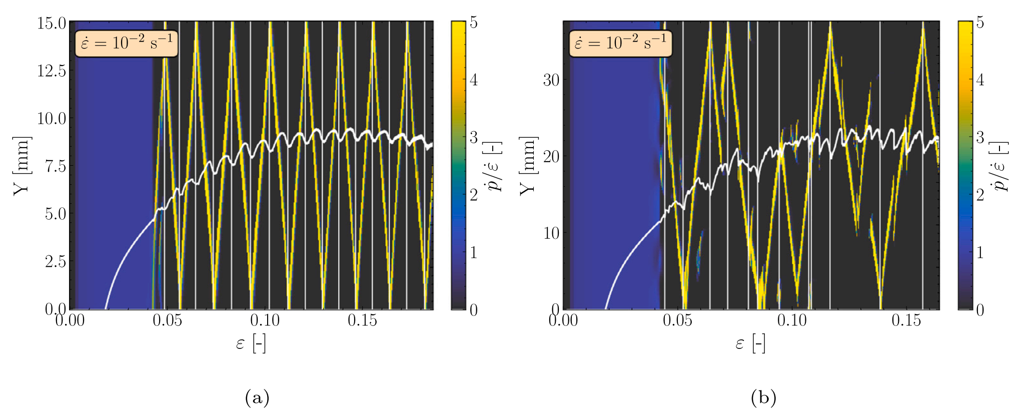

Fig. 17. Spatio-temporal visualisation of PLC band dynamics in simulated plates deformed at $\dot{\varepsilon} = 10^{-2}$ s^{-1}. (a) Standard plate ($10 \times 15 \times 2$ mm). (b) Extended plate ($10 \times 37.5 \times 2$ mm). The correlation between stress drops and band reflection events are highlighted with white lines. Stress drops are also observed during band relocalisation across the specimen. (For interpretation of the references to colour in this figure legend, the reader is referred to the web version of this article.)

18(d), highlighting the correlation between the variations in t_a and $\dot{p}$ and the emergence of serrations.

For the two considered strain rates, the evolution of the plastic strain rate and ageing time stabilise towards a repeating pattern characteristic of a limit cycle which in turns governs the dynamics of serrations. Two key phases emerge in their joint dynamics:

- **Locking Phase:** Characterised by a decrease in $\dot{p}$ and a corresponding increase in t_a. This behaviour arises from the relaxation law Eq. (8), which for vanishing $\dot{p}$ gives $\dot{t}_a \approx 1$, implying a near-linear growth of t_a. Notably, the maximum values attained by t_a decrease with increasing strain rate due to the reduced timescales.
- **Stall Phase:** As t_a approaches a critical threshold, the bifurcation criterion is met, triggering a rapid increase in $\dot{p}$ in a localised region. Despite the intense plastic flow, t_a remains almost constant, until $\dot{p}$ stabilises, after which $\dot{t}_a$ decreases. Physically, this corresponds to the phase of unpinning of the dislocations, resulting in a serration on the stress curve.

The dynamics of the attractor itself reveal the hallmarks of chaotic systems: alternating phases of rapid expansion (stall) and contraction (locking), resulting in the stretching and folding mechanisms responsible for chaos.

An additional feature appears at low strain rates, as seen in Fig. 18(a), where a secondary sub-cycle arises. This occurs when a plastic localisation event develops outside the observed Gauss points. Here, $\dot{p}$ spikes momentarily and stabilises while $\dot{t}_a \sim 0$, resulting in a minor decrease in t_a. Depending on the intensity of the localisation, $\dot{p}$ may either rise again or settle into a new equilibrium.

The evolution of the equivalent stress σ can be visualised as a function of plastic strain p and plastic strain rate $\dot{p}$ under the assumption

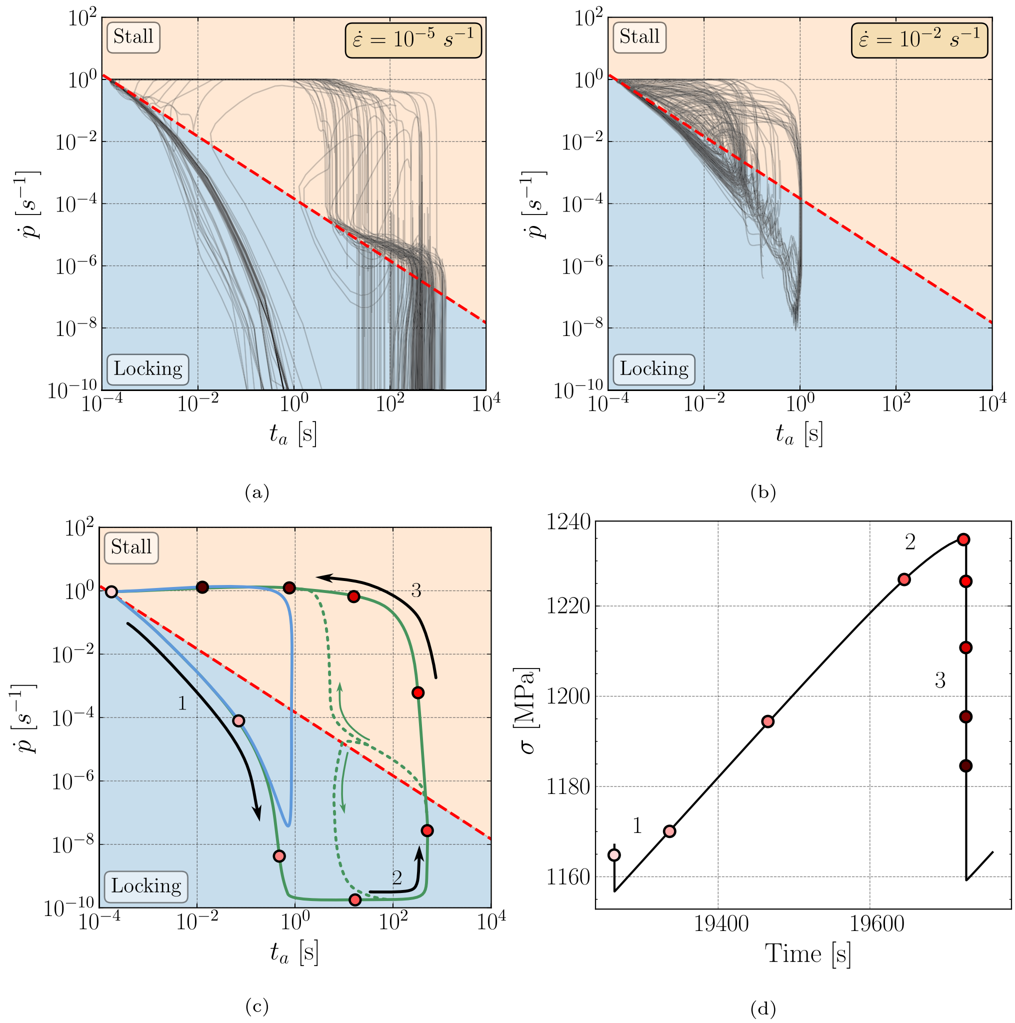

Fig. 18. Phase space of the KEMC model at Gauss points for strain rates (a) 10^{-5} s^{-1} and (b) 10^{-2} s^{-1} in the plastic strain interval $p \in [0.11, 0.12]$. The red line indicates the relationship between t_a and $\dot{p}$ under the condition $\dot{t}_a = 0$. To improve clarity, values of $\dot{p} < 10^{-10}$ s^{-1} have been excluded. A saturation of $\dot{p}$ is observed near 1 s^{-1}, stemming from a built-in constraint in the Z-set solver designed to maintain numerical integration stability. (c) Schematic representation of the phase space at low (green) and high (blue) strain rates. (d) Example of serration dynamics showing the evolution of phase space trajectories characteristic of type C serrations. (For interpretation of the references to colour in this figure legend, the reader is referred to the web version of this article.)

that the internal variable t_a has reached a steady state, $\dot{t}_a = 0$. The resulting 3D surface is shown in Figs. 19(a) and 19(b), for strain rates $\dot{\varepsilon} = 10^{-5}$ s^{-1} and $\dot{\varepsilon} = 10^{-2}$ s^{-1} respectively. This representation captures the combined effects of R_v, R_h, and R_a (cf. Eqs. (5)–(7)), offering insight into the inverse sensitivity behaviour modelled by the system. Superimposed on this surface is the stress evolution at a Gauss point for both stable and unstable configurations, with the colour map representing the strain rate sensitivity.

The KEMC model successfully reproduces the characteristic hysteresis loop of the PLC effect predicted by the theoretical framework of Penning (1972), Kubin et al. (1988). This loop unfolds as follows:

1. Sharp increase in strain rate, associated with a jump over NSRS valley.
2. Drop in stress associated with the dislocation unpinning or stall phase.
3. Sudden reduction in strain rate, indicating renewed dislocation-atmosphere interactions.
4. Elastic reloading of the material.

This representation allows us to visualise how the attractor's dynamics evolves on the characteristic stress surface. In Fig. 19(a), the stress at Gauss points lies on the equilibrium surface for low $\dot{p}$, indicating that the model has reached the saturation of t_a. At higher strain rates, however, this saturation is not achieved, as shown in Fig. 18(b), where the stress evolves along a curve of lower magnitude than the surface.

Fundamentally, observing the complete evolution of the intrinsic curve in the model's phase space would require accounting for all variables of interest $(\sigma, p, \dot{p}, t_a)$, which is impractical as it demands a 4D representation. Moreover, the characteristic surface shown in Fig. 19 only represents the equilibrium state reached when the system is fully aged, and thus fails to capture out-of-equilibrium conditions. To address this limitation, we propose a new representation that displays stress evolution on a strain-rate and ageing-time-dependent surface, as illustrated in Figs. 20(a) and 20(b). This approach generalises the phase space representation of Fig. 18 to better encompass the system's dynamic behaviour.

The surfaces provide a clear picture of the mechanics underlying the serrations in the PLC effect. During periods of low plastic activity, the material undergoes ageing, and the ageing stress increases. When local conditions favour the onset of a serration, the strain rate increases and the ageing time t_a decreases, signifying the unpinning of dislocations. Consequently, the ageing stress drops, producing the characteristic serration. This process stops when $\dot{t}_a$ returns to zero, indicating that dislocations have sufficiently detached from solute atmospheres. When

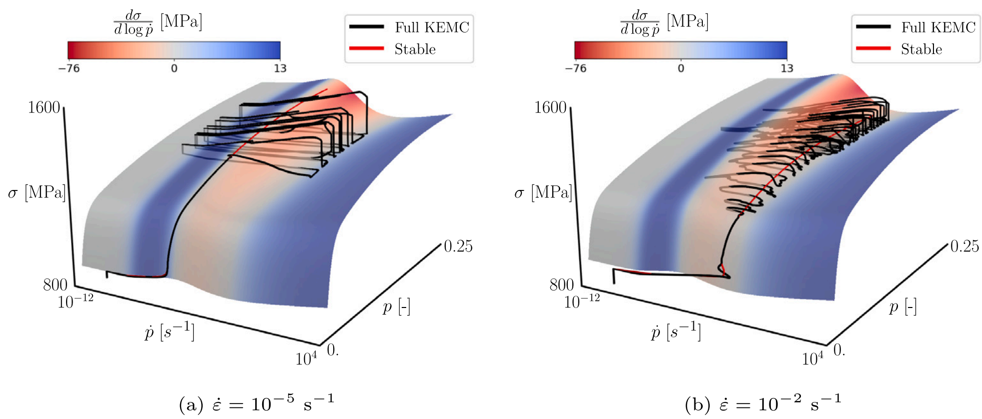

Fig. 19. Evolution of the equivalent stress at a Gauss point on the representative stress surface of the KEMC model in function of plastic strain and strain rate, for applied strain rate (a) 10^{-5} s^{-1} (b) 10^{-2} s^{-1}. The colourmap is representative of the strain rate sensitivity. We observe the characteristic hysteresis of the PLC effect. (For interpretation of the references to colour in this figure legend, the reader is referred to the web version of this article.)

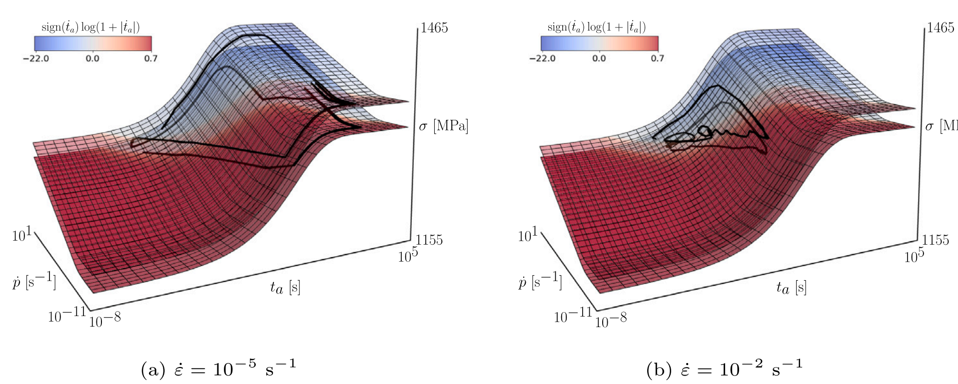

Fig. 20. Evolution of the equivalent stress at a Gauss point on the representative stress surface of the KEMC constitutive law as a function of ageing time and strain rate, under applied strain rates in the plastic regime (a) $\dot{\varepsilon} = 10^{-5}$ s^{-1} over $p \in [0.087, 0.107]$, (b) $\dot{\varepsilon} = 10^{-2}$ s^{-1} over $p \in [0.087, 0.104]$. To account for the evolving nature of the surface with plastic strain, both the initial and final surfaces within the specified intervals are shown. The colour map indicates the time derivative of the ageing time ($\dot{t}_a$). The hysteresis of the model is clearly visible in the evolution of the surfaces, highlighting that the amplitude of stress drops is dependent on the effective ageing time. (For interpretation of the references to colour in this figure legend, the reader is referred to the web version of this article.)

$\dot{t}_a > 0$, the pinning process restarts, and the ageing stress rises once again.

From this perspective, the timescales involved have a direct impact on the ageing kinetics and thus on the dynamics of serrations. Broadly speaking, the time between two successive serrations consists of the elastic reloading time, or total ageing time t_L, and a plastic relaxation time t_p, which corresponds to the duration of the stress drop during which a plastic strain increment $\Delta\varepsilon^p$ is accommodated. In practice, the duration of a serration is short, so we can approximate:

$$\Delta t \simeq t_L \simeq \frac{\Delta\varepsilon}{\dot{\varepsilon}_0} \tag{23}$$

On average, it is observed that a stress drop roughly carries $\Delta\varepsilon \simeq 0.2\%$ of plastic strain. For a tensile test conducted at $\dot{\varepsilon}_0 = 10^{-5}\,\text{s}^{-1}$, this yields $\Delta t \simeq 2\times10^4$ s. This extended timescale allows the ageing process to fully develop, leading to the formation of high-intensity serrations. Conversely, at $\dot{\varepsilon}_0 = 10^{-2}\,\text{s}^{-1}$, we find $\Delta t \simeq 20$ s. As a consequence, the ageing stress cannot reach saturation, as seen in Fig. 20(b). To accommodate the imposed displacement, plastic relaxation needs to happen more frequently, leading to serrations of lower magnitude and promoting the continuous propagation of plastic bands.

Using similar arguments, one can estimate the magnitude of stress drops in systems where the machine's rigidity is of the same order of magnitude as the specimen's stiffness. Approximating the stress rate by $\dot{\sigma} \simeq \Delta\sigma/\Delta t$, the machine equation Eq. (22) simplifies to:

$$\Delta\sigma = \frac{KL}{S}(1-f)\,\Delta\varepsilon, \tag{24}$$

Here, f denotes the fraction of the gauge length over which the plastic band localises, and depends on the band propagation mode. The parameter K represents the machine stiffness. For a tensile test conducted at a strain rate of $\dot{\varepsilon} = 10^{-4}$ s^{-1}, using the machine stiffness determined in Section 5.2, and a specimen with dimensions $L = 15$ mm and $S = 20$ mm^2 as described in Section 2.2, a band fraction of $f = 0.15$ and strain drop increments of $\Delta\varepsilon \simeq 0.2\%$ yield a stress drop of $\Delta\sigma \simeq 47$ MPa, which falls within the same range as the average stress drop observed in Fig. 10(a) for the corresponding strain rate.

7. Conclusion

This study presents a comprehensive experimental and numerical investigation of the PLC effect in a nickel-based superalloy. The main findings are summarised as follows:

1. The finite element simulations based on the KEMC model successfully reproduce the complex spatio-temporal dynamics of the PLC effect, including the evolution of serrations statistics with

strain rate. A stabilised version of the model enables simulations without serrations while preserving the negative strain rate sensitivity. It is found that the model generates lower-dimensional attractors than experimental data and overestimates multifractal indicators. This suggests that additional internal variables and finer-scale dynamics are needed for complete representation of the phenomenon. In this context, a transition to crystal plasticity framework might be the needed ingredient, to refine the model and take into account other barriers to the band propagation such as grain boundaries (Marchenko et al., 2016).
2. The machine stiffness plays a crucial role in shaping serration morphology and dynamics, affecting mean amplitudes, periods of stress drops, and dynamical indicators (correlation dimension, Lyapunov exponent). These computational findings align with experimental observations.
3. Experimental data consistently show chaotic dynamics across all strain rates with no evidence of self-organised criticality (SOC), correlating with type B and C serrations. Chaotic dynamics is also observed in the simulations. They are associated with the expression of type B and C serrations. On the other hand, type A bands are predicted at high strain rates by the model and correlated with SOC-like dynamics. A power-law relationship is exhibited between average serration amplitudes and strain rate. This behaviour is observed in both simulations and experiments where each critical exponent is associated to its related dynamical behaviour.
4. Statistical, dynamical, and multifractal indicators provide consistent and correlated trends reflecting serration dynamics evolution. These indicators collectively capture the transition from chaotic behaviour to SOC as strain rate increases (type B to type A bands). They serve as reliable quantitative metrics for characterising deformation regimes.
5. Sharp stress drops arise from both plastic localisation and band-geometry interactions. In particular, the diffusion or reflection of type A bands into the specimen fillets lead to the major serrations on the stress–strain curves. Plastic strain rate distributions in spatio-temporal diagrams follow power-laws with consistent critical exponents across strain rates, while multifractality is strongest at low strain rates corresponding to more erratic dynamics.
6. The analysis of material point individual responses reveals attractors governing stress fluctuations, with equivalent stress evolving on characteristic KEMC model surfaces that reproduce PLC hysteresis, directly correlating band dynamics to effective ageing time, as depicted in the phase spaces.
7. A stabilised version of the KEMC model was proposed, that properly accounts for the negative strain rate sensitivity of the material in the considered temperature and strain rate ranges, but gets rid of serrations. This stabilised model can be useful for engineering applications to industrial components where detailed description of PLC bands is generally not necessary. The approach, based on a bifurcation analysis *on the fly*, has the advantage of keeping the complete KEMC model until first instabilities can occur.

These results confirm the KEMC model's ability to capture quantitatively the essential features of the PLC effect in a nickel-based superalloys. They highlight the critical role played by machine stiffness, specimen geometry, and internal material dynamics in shaping the observed behaviour. The use of statistical and dynamical indicators proves particularly valuable for assessing whether the simulated dynamics rightfully reproduce experimentally observed behaviours. Such indicators could be integrated into cost functions to improve parameter identification for constitutive models. Moreover, they offer promising prospects for use in experimental techniques — such as digital image correlation — providing new avenues for detailed characterisation of complex deformation dynamics. It is observed that similar band types give rise to comparable dynamic behaviours in both nickel-based superalloys and aluminium alloys. This convergence suggests the possibility of universal features in the dynamics of PLC bands. However, broader investigations involving a wider range of materials are needed to further assess the extent of this potential universality.

CRediT authorship contribution statement

Florian Billon: Writing – original draft, Visualization, Validation, Software, Resources, Methodology, Investigation, Formal analysis, Data curation, Conceptualization. **Aurélien Vattré:** Writing – review & editing, Validation, Project administration, Investigation, Funding acquisition, Formal analysis, Data curation, Conceptualization. **Sylvain Zambelli:** Writing – review & editing, Validation, Supervision, Project administration, Methodology, Investigation, Funding acquisition, Formal analysis, Data curation, Conceptualization. **Matthieu Mazière:** Writing – review & editing, Validation, Supervision, Methodology, Investigation, Funding acquisition, Formal analysis, Data curation, Conceptualization. **Samuel Forest:** Writing – review & editing, Validation, Supervision, Software, Resources, Project administration, Methodology, Investigation, Funding acquisition, Formal analysis, Data curation, Conceptualization.

Declaration of competing interest

The authors declare that they have no known competing financial interests or personal relationships that could have appeared to influence the work reported in this paper.

Acknowledgements

The authors thank Dr. Moubine Al Kotob for support, stimulating discussions and initiative of this study.

Appendix. Stability analysis of the KEMC model

The critical conditions for the emergence of PLC viscoplastic instabilities are derived analytically from the KEMC model through a bifurcation analysis according to Mesarovic (1995). The criteria are then used to identify the critical plastic strain ε^c at which the first serration of the tensile test can occurs. Beforehand, two hypotheses, which will remain true up to the critical strain, are made:

- The mechanical behaviour of the specimen is equivalent to the behaviour of a volume element under uniaxial tension.
- $\dot{p}$ is constant during the simulation and t_a is at saturation, i.e, $\dot{t}_a = 0$.

Under plastic loading conditions, the tensile stress is expressed as:

$$\sigma = R_h(p) + R_v(\dot{p}) + R_a(p, t_a) \tag{A.1}$$

where R_h, R_v and R_a are the hardening, viscous and ageing parts of the stress, respectively. According to Eq. (8) the ageing time is expressed as:

$$t_a = \frac{w}{\dot{p}} \tag{A.2}$$

The bifurcation criterion is derived by introducing a small exponential perturbation in the set of equations. It is assumed, that the solution of the perturbed system is written as the product of space and time functions:

$$\delta[\mathbf{X}(x,t)] = \left[X_0(x)\right] \exp(\lambda t) = \begin{bmatrix} \delta p \\ \delta t_a \\ \delta\sigma \end{bmatrix} \tag{A.3}$$

where, λ is the *Lyapunov exponent* of the system. Its value is deeply related to the stability of the system and the growth or decay of the perturbation. By introducing the perturbation in the set of equations, we obtain the following system:

$$\begin{cases} \delta\sigma = \dfrac{dR_h(p)}{dp}\delta p + \dfrac{\partial R_a\left(p,t_a\right)}{\partial p}\delta p + \dfrac{\partial R_a\left(p,t_a\right)}{\partial t_a}\delta t_a + \dfrac{dR_v(\dot{p})}{d\dot{p}}\delta\dot{p} & \text{(A.4)} \\ w\delta\dot{t}_a = -\left(\dfrac{\delta\left(t_a\dot{p}\right)}{\delta t_a}\delta t_a + \dfrac{\delta\left(t_a\dot{p}\right)}{\delta\dot{p}}\delta\dot{p}\right) = -t_a\delta\dot{p} - \dot{p}\delta t_a & \text{(A.5)} \\ \delta\sigma = \sigma\delta p & \text{(A.6)} \end{cases}$$

Eq. (A.6) is related to the condition of plastic necking also known as the Considère criterion. By combining, Eq. (A.4) and (A.6) we obtain:

$$\delta\dot{p} = \left(\frac{dR_v(\dot{p})}{\dot{p}}\right)^{-1}\left[\left(\sigma - \frac{dR_hard(p)}{dp} - \frac{\partial R_a\left(p,t_a\right)}{\partial p}\right)\delta p - \frac{\partial R_a\left(p,t_a\right)}{\partial t_a}\delta t_a\right] \tag{A.7}$$

The system of equation Eq. (A.5) and (A.7) is then rewritten in matrix form:

$$\begin{bmatrix} \delta\dot{p} \\ \delta\dot{t}_a \end{bmatrix} = \frac{\dot{p}}{S_i}\begin{bmatrix} (\sigma - \Theta) & \frac{S_a}{t_a} \\ \frac{t_a}{w}(\Theta - \sigma) & -\frac{1}{w}\left(S_i + S_a\right) \end{bmatrix} \cdot \begin{bmatrix} \delta p \\ \delta t_a \end{bmatrix} = \mathbf{M}\cdot\begin{bmatrix} \delta p \\ \delta t_a \end{bmatrix} \tag{A.8}$$

where,

$$\begin{cases} S = S_i + S_a, & \Theta = \dfrac{dR}{dp} + \dfrac{\partial R_a}{\partial p} \\ S_i = \dot{p}\dfrac{dR_v}{d\dot{p}}, & S_a = -t_a\dfrac{\partial R_a}{\partial t_a} \end{cases} \tag{A.9}$$

M is a 2×2 matrix subjected to a spectral analysis. Its eigenvalues, corresponding to the Lyapunov exponents, characterise the stability of the system. They are determined straightforwardly from the characteristic equation of the matrix. We have,

$$\begin{cases} \mathrm{Tr}(\mathbf{M}) = -\dfrac{\dot{p}}{wS_i}[S + w(\Theta - \sigma)] & \text{(A.10)} \\ \det(\mathbf{M}) = \left(\dfrac{\dot{p}}{S_i}\right)^2\dfrac{(\Theta - \sigma)}{w}S_i & \text{(A.11)} \\ \lambda^2 - \mathrm{Tr}(\mathbf{M})\lambda + \det(\mathbf{M}) = 0 & \text{(A.12)} \end{cases}$$

Two eigenvalues can be obtained from Eq. (A.12). They depend on the discriminant of the characteristic equation, derived as:

$$\begin{aligned} \Delta(\mathbf{M}) &= \mathrm{Tr}(\mathbf{M})^2 - 4\det(\mathbf{M}) \\ &= \left(\frac{\dot{p}}{wS_i}\right)^2\left[(S + w(\Theta - \sigma))^2 - 4w(\Theta - \sigma)S_i\right] \end{aligned} \tag{A.13}$$

Two cases are identified to observe the growth of the perturbation:

- $\Delta(\mathbf{M}) < 0$ and $\mathrm{Tr}(\mathbf{M}) > 0$: the eigenvalues are complex with a positive real part. The perturbation grows by oscillating.
- $\Delta(\mathbf{M}) > 0$ and $\mathrm{Tr}(\mathbf{M}) > 0$: the eigenvalues are real and positive. The perturbation grows exponentially.

Therefore, this analysis provides two different stability criteria. The first one is the oscillating growth criterion (OGC):

$$S_{\mathrm{OCG}} = S + w(\Theta - \sigma) < 0 \tag{A.14}$$

The second one is the exponential growth criterion (EGC):

$$S_{\mathrm{EGC}} = S + w(\Theta - \sigma) + 2\sqrt{w(\Theta - \sigma)S_i} < 0 \tag{A.15}$$

also expressed as:

$$S_{EGC} = \begin{cases} \left(S_{\mathrm{OGC}}\right)^2 - 4w(\Theta - \sigma)S_i < 0 \quad \text{and,} \\ S_{\mathrm{OGC}} < 0 \end{cases} \tag{A.16}$$

The EGC is fulfilled at a higher value of plastic strain than the OGC. Numerical investigation (Mazière and Dierke, 2012), showed that the EGC appears to be the most relevant criterion to predict the occurrence of the first serration during a numerical simulation, as compared to experimental observations.

Appendix B. Supplementary data

Supplementary material related to this article can be found online at https://doi.org/10.1016/j.euromechsol.2026.106068.

Data availability

Data will be made available on request.

References

Abry, P., Jaffard, S., Wendt, H., 2012. Irregularities and scaling in signal and image processing: multifractal analysis. arXiv:1210.0482.

Ananthakrishna, G., Fressengeas, C., Grosbras, M., Vergnol, J., Engelke, C., Plessing, J., Neuhäuser, H., Bouchaud, E., Planès, J., Kubin, L.P., 1995. On the existence of chaos in jerky flow. Scr. Met. Mater. 32 (11), 1731–1737. http://dx.doi.org/10.1016/0956-716X(95)00013-L.

Ananthakrishna, G., Valsakumar, M.C., 1982. Repeated yield drop phenomenon: A temporal dissipative structure. J. Phys. D: Appl. Phys. 15 (12), L171–L175. http://dx.doi.org/10.1088/0022-3727/15/12/003.

Arnold, V.I., 1992. Catastrophe Theory. Springer Berlin, Heidelberg, http://dx.doi.org/10.1007/978-3-642-58124-3.

Bak, P., Tang, C., Wiesenfeld, K., 1988. Self-organized criticality. Phys. Rev. A 38, 364–374. http://dx.doi.org/10.1103/PhysRevA.38.364.

Belotteau, J., Berdin, C., Forest, S., Parrot, A., Prioul, C., 2009. Mechanical behavior and crack tip plasticity of a strain aging sensitive steel. Mater. Sci. Eng.: A 526 (1–2), 156–165. http://dx.doi.org/10.1016/j.msea.2009.07.013.

Benallal, A., Berstad, T., Børvik, T., Clausen, A., Hopperstad, O., 2006. Dynamic strain aging and related instabilities: experimental, theoretical and numerical aspects. Eur. J. Mech. A Solids 25 (3), 397–424. http://dx.doi.org/10.1016/j.euromechsol.2005.10.007.

Benallal, A., Berstad, T., Børvik, T., Hopperstad, O.S., Koutiri, I., De Codes, R.N., 2008. An experimental and numerical investigation of the behaviour of AA5083 aluminium alloy in presence of the Portevin-Le Chatelier effect. Int. J. Plast. 24 (10), 1916–1945.

Besson, J., Cailletaud, G., Chaboche, J.L., Forest, S., Blétry, M., 2012. Non-Linear Mechanics of Materials. Springer.

Bharathi, M.S., Ananthakrishna, G., 2003. Dynamics of crossover from a chaotic to a power law state in jerky flow. Phys. Rev. E 67 (6), 065104. http://dx.doi.org/10.1103/PhysRevE.67.065104.

Bharathi, M.S., Lebyodkin, M., Ananthakrishna, G., Fressengeas, C., Kubin, L.P., 2001. Multifractal burst in the spatiotemporal dynamics of jerky flow. Phys. Rev. Lett. 87 (16), 165508.

Bharathi, M., Lebyodkin, M., Ananthakrishna, G., Fressengeas, C., Kubin, L., 2002. The hidden order behind jerky flow. Acta Mater. 50 (11), 2813–2824. http://dx.doi.org/10.1016/S1359-6454(02)00099-X.

Blanc, D., Strudel, J.L., 1985. Dynamic strain ageing and relaxation in 316 type stainless steel. In: Mcqueen, H.J., Bailon, J.P., Dickson, J.I., Jonas, J.J., Akben, M.G. (Eds.), Strength of Metals and Alloys. ICSMA 7, Pergamon, pp. 349–354. http://dx.doi.org/10.1016/B978-0-08-031642-0.50065-9.

Böhlke, T., Bondar, G., Estrin, Y., Lebyodkin, M.A., 2009. Geometrically non-linear modeling of the Portevin-Le Chatelier effect. Comput. Mater. Sci. 44 (4), 1076. http://dx.doi.org/10.1016/j.commatsci.2008.07.036.

Van den Brink, S.H., Van den Beukel, A., McCormick, P.G., 1977. The influence of specimen dimensions and machine stiffness on the Portevin-Le Chatelier effect in an Al–Cu alloy. Phys. Status Solidi (A) 41 (2), 513–521. http://dx.doi.org/10.1002/pssa.2210410222.

Broomhead, D.S., King, G.P., 1986. Extracting qualitative dynamics from experimental data. Phys. D: Nonlinear Phenom. 20 (2), 217–236. http://dx.doi.org/10.1016/0167-2789(86)90031-X.

Cao, L., 1997. Practical method for determining the minimum embedding dimension of a scalar time series. Phys. D: Nonlinear Phenom. 110 (1), 43–50. http://dx.doi.org/10.1016/S0167-2789(97)00118-8.

Chen, K., Bak, P., Jensen, M.H., 1990. A deterministic critical forest fire model. Phys. Lett. A 149 (4), 207–210.

Cuddy, L.J., Leslie, W.C., 1972. Some aspects of serrated yielding in substitutional solid solutions of iron. Acta Metall. 20 (10), 1157–1167. http://dx.doi.org/10.1016/0001-6160(72)90164-2.

Curtin, W.A., Olmsted, D.L., Hector, L.G., 2006. A predictive mechanism for dynamic strain ageing in aluminium–magnesium alloys. Nat. Mater. 5 (11), 875–880. http://dx.doi.org/10.1038/nmat1765.

Eckmann, J.P., Kamphorst, S.O., Ruelle, D., Ciliberto, S., 1986-12-01. Liapunov exponents from time series. Phys. Rev. A 34 (6), 4971–4979. http://dx.doi.org/10.1103/PhysRevA.34.4971.

Fressengeas, C., Beaudoin, A.J., Lebyodkin, M., Kubin, L.P., Estrin, Y., 2005. Dynamic strain aging: A coupled dislocation-solute dynamic model. Dislocations 2004, Mater. Sci. Eng.: A Dislocations 2004, 400–401, 226–230.http://dx.doi.org/10.1016/j.msea.2005.02.073,

Frisch, U., Parisi, G., 1980. Fully developed turbulence and intermittency. N. Y. Acad. Sci. Ann. 357, 359–367.

Graff, S., Dierke, H., Forest, S., Neuhäuser, H., Strudel, J.L., 2008. Finite element simulations of the Portevin-Le Chatelier effect in metal-matrix composites. Phil. Mag. 88 (28–29), 3389–3414. http://dx.doi.org/10.1080/14786430802108472.

Graff, S., Forest, S., Strudel, J.L., Prioul, C., Pilvin, P., Béchade, J.L., 2004. Strain localization phenomena associated with static and dynamic strain ageing in notched specimens: Experiments and finite element simulations. Mater. Sci. Eng.: A 387–389, 181–185. http://dx.doi.org/10.1016/j.msea.2004.02.083.

Grassberger, P., Procaccia, I., 1983. Measuring the strangeness of strange attractors. Phys. D: Nonlinear Phenom. 9 (1), 189–208. http://dx.doi.org/10.1016/0167-2789(83)90298-1.

Guillermin, N., Besson, J., Köster, A., Lacourt, L., Mazière, M., Chalons, H., Forest, S., 2023. Experimental and numerical analysis of the Portevin–Le Chatelier effect in a nickel-base superalloy for turbine disks application. Int. J. Solids Struct. 264, 112076. http://dx.doi.org/10.1016/j.ijsolstr.2022.112076.

Hentschel, H., Procaccia, I., 1983. The infinite number of generalized dimensions of fractals and strange attractors. Phys. D: Nonlinear Phenom. 8 (3), 435–444. http://dx.doi.org/10.1016/0167-2789(83)90235-X.

Hosford, W.F., 1972. A generalized isotropic yield criterion. J. Appl. Mech. 39 (2), 607–609. http://dx.doi.org/10.1115/1.3422732.

Jaffard, S., 2004. Wavelet techniques in multifractal analysis. In: Proceedings of Symposia in Pure Mathematics, vol. 72, no. 2, pp. 91–152.

Jaffard, S., Lashermes, B., Abry, P., 2006. Wavelet leaders in multifractal analysis. In: Wavelet Analysis and Applications. Birkhäuser, Basel, Switzerland, pp. 201–246.

Kantelhardt, J.W., Zschiegner, S.A., Koscielny-Bunde, E., Havlin, S., Bunde, A., Stanley, H., 2002. Multifractal detrended fluctuation analysis of nonstationary time series. Phys. A 316 (1), 87–114. http://dx.doi.org/10.1016/S0378-4371(02)01383-3.

Klose, F.B., Ziegenbein, A., Hagemann, F., Neuhäuser, H., Hähner, P., Abbadi, M., Zeghloul, A., 2004. Analysis of Portevin-Le Chatelier serrations of type b in Al-Mg. Mater. Sci. Eng.: A 369 (1), 76–81. http://dx.doi.org/10.1016/j.msea.2003.10.292.

Klusemann, B., Fischer, G., Böhlke, T., Svendsen, B., 2015. Thermomechanical characterization of Portevin–Le Châtelier bands in AlMg3 (AA5754) and modeling based on a modified Estrin–McCormick approach. Int. J. Plast. 67, 192–216. http://dx.doi.org/10.1016/j.ijplas.2014.10.011.

Kok, S., Bharathi, M.S., Beaudoin, A.J., Fressengeas, C., Ananthakrishna, G., Kubin, L.P., Lebyodkin, M., 2003. Spatial coupling in jerky flow using polycrystal plasticity. Acta Mater. (13), 3651–3662. http://dx.doi.org/10.1016/S1359-6454(03)00114-9.

Kubin, L.P., Chihab, K., Estrin, Y., 1988. The rate dependence of the Portevin-Le Chatelier effect. Acta Metall. 36 (10), 2707–2718. http://dx.doi.org/10.1016/0001-6160(88)90117-4.

Kubin, L.P., Estrin, Y., 1985. The Portevin-Le Chatelier effect in deformation with constant stress rate. Acta Metall. 33 (3), 397–407. http://dx.doi.org/10.1016/0001-6160(85)90082-3.

Kubin, L.P., Estrin, Y., 1990. Evolution of dislocation densities and the critical conditions for the Portevin-Le Chatelier effect. Acta Met. Mater. 38 (5), 697–708. http://dx.doi.org/10.1016/0956-7151(90)90021-8.

Lebyodkin, M.A., Brechet, Y., Estrin, Y., Kubin, L.P., 1995. Statistics of the catastrophic slip events in the Portevin–Le Chatelier effect. Phys. Rev. Lett. 74 (23), 4758–4761. http://dx.doi.org/10.1103/PhysRevLett.74.4758.

Lebyodkin, M., Dunin-Barkowskii, L., Bréchet, Y., Estrin, Y., Kubin, L., 2000. Spatio-temporal dynamics of the Portevin–Le Chatelier effect: Experiment and modelling. Acta Mater. 48 (10), 2529–2541. http://dx.doi.org/10.1016/S1359-6454(00)00067-7.

Lebyodkin, M.A., Estrin, Y., 2005. Multifractal analysis of the Portevin–Le Chatelier effect: general approach and application to AlMg and AlMg/Al2O3 alloys. Acta Mater. 53 (12), 3403–3413. http://dx.doi.org/10.1016/j.actamat.2005.03.042.

Lebyodkin, M.A., Shashkov, I.V., Lebedkina, T.A., Gornakov, V.S., 2017. Experimental investigation of the effect of thresholding on temporal statistics of avalanches. Phys. Rev. E 95, 032910. http://dx.doi.org/10.1103/PhysRevE.95.032910.

Ling, C.P., McCormick, P.G., 1993. The effect of temperature on strain rate sensitivity in an Al Mg Si alloy. Acta Met. et Mater. 41 (11), 3127–3131. http://dx.doi.org/10.1016/0956-7151(93)90042-Q.

Luo, S., Xiao, L., Jiang, J., Li, J., Zeng, L., 2024. Influence of machine stiffness on the Portevin–Le Chatelier effect of Ti-12Mo alloy based on a modified McCormick constitutive model. Met. Mater. Int. http://dx.doi.org/10.1007/s12540-024-01669-x.

Marchenko, M., Mazière, M., Forest, S., Strudel, J.L., 2016. Crystal plasticity simulation of strain aging phenomena in alpha-titanium at room temperature. Int. J. Plast. 85, 1–33. http://dx.doi.org/10.1016/j.ijplas.2016.05.007.

Mazière, M., Besson, J., Forest, S., Tanguy, B., Chalons, H., Vogel, F., 2009. Overspeed burst of elastoviscoplastic rotating disks part II: Burst of a superalloy turbine disk. Eur. J. Mech. A Solids 28, 428–432.

Mazière, M., Besson, J., Forest, S., Tanguy, B., Chalons, H., Vogel, F., 2010a. Numerical aspects in the finite element simulation of the Portevin–Le Chatelier effect. Comput. Methods Appl. Mech. Engrg. 199 (9–12), 734–754. http://dx.doi.org/10.1016/j.cma.2009.11.004.

Mazière, M., Dierke, H., 2012. Investigations on the Portevin Le Chatelier critical strain in an aluminum alloy. Comput. Mater. Sci. 52 (1), 68–72. http://dx.doi.org/10.1016/j.commatsci.2011.05.039.

Mazière, M., Forest, S., Besson, J., Wang, H., Berdin, C., 2010b. Numerical simulation of the Portevin Le Chatelier effect in various materials and at different scales. Mater. Sci. Forum 638–642, 2670–2675.

McCormick, P., 1988. Theory of flow localisation due to dynamic strain ageing. Acta Metall. 36 (12), 3061–3067. http://dx.doi.org/10.1016/0001-6160(88)90043-0.

Mesarovic, S.D., 1995. Dynamic strain aging and plastic instabilities. J. Mech. Phys. Solids 43 (5), 671–700. http://dx.doi.org/10.1016/0022-5096(95)00010-G.

Muzy, J.F., Bacry, E., Arneodo, A., 1993. Multifractal formalism for fractal signals: The structure-function approach versus the wavelet-transform modulus-maxima method. Phys. Rev. E 47, 875–884. http://dx.doi.org/10.1103/PhysRevE.47.875.

Penning, P., 1972. Mathematics of the Portevin-Le Chatelier effect. Acta Metall. 20 (10), 1169–1175. http://dx.doi.org/10.1016/0001-6160(72)90165-4.

Picu, R.C., 2004. A mechanism for the negative strain-rate sensitivity of dilute solid solutions. Acta Mater. 52 (12), 3447–3458. http://dx.doi.org/10.1016/j.actamat.2004.03.042.

Ranc, N., Wagner, D., 2005. Some aspects of Portevin–Le Chatelier plastic instabilities investigated by infrared pyrometry. Mater. Sci. Eng.: A 394 (1), 87–95. http://dx.doi.org/10.1016/j.msea.2004.11.042.

Reed, R.C., 2006. The Superalloys: Fundamentals and Applications. Cambridge University Press.

Ren, S., Mazière, M., Forest, S., Morgeneyer, T.F., Rousselier, G., 2017. A constitutive model accounting for strain ageing effects on work-hardening. Application to a C–Mn steel. C. R. Méc. 345, 908–921. http://dx.doi.org/10.1016/j.crme.2017.09.005.

Rizzi, E., Hähner, P., 2004. On the Portevin–Le Chatelier effect: Theoretical modeling and numerical results. Int. J. Plast. 20 (1), 121–165. http://dx.doi.org/10.1016/S0749-6419(03)00035-4.

Rodriguez, P., 1984. Serrated plastic flow. Bull. Mater. Sci. 6 (4), 653–663. http://dx.doi.org/10.1007/BF02743993.

Rosenstein, M.T., Collins, J.J., De Luca, C.J., 1993. A practical method for calculating largest Lyapunov exponents from small data sets. Phys. D: Nonlinear Phenom. 65 (1), 117–134. http://dx.doi.org/10.1016/0167-2789(93)90009-P.

Rowlands, B.S., Rae, C., Galindo-Nava, E., 2023. The Portevin-Le Chatelier effect in nickel-base superalloys: origins, consequences and comparison to strain ageing in other alloy systems. Prog. Mater. Sci. 132, 101038. http://dx.doi.org/10.1016/j.pmatsci.2022.101038.

Schuster, H.G., 1988. Deterministic Chaos: An Introduction. VCH.

Sleeswyk, A.W., 1958. Slow strain-hardening of ingot iron. Acta Metall. 6 (9), 598–603. http://dx.doi.org/10.1016/0001-6160(58)90101-9.

Song, R.H., Qin, H.L., Bi, Z.N., Zhang, J., Chi, H., Busso, E.P., Li, D.F., 2020. Experimental and numerical investigations of dynamic strain ageing behaviour in solid solution treated inconel 718 superalloy. Eng. Comput. 38, 19–35. http://dx.doi.org/10.1108/EC-01-2020-0006.

Strogatz, S., 2019. Nonlinear dynamics and chaos: With applications to physics, biology, chemistry, and engineering, second ed., first issued in hardback In: A Chapman & Hall Book, CRC Press, Boca Raton London New York.

Takens, F., 1981. Detecting strange attractors in turbulence. In: Rand, D., Young, L.S. (Eds.), In: Dynamical Systems and Turbulence, Warwick 1980, vol. 898, Springer Berlin Heidelberg, Berlin, Heidelberg, pp. 366–381. http://dx.doi.org/10.1007/BFb0091924.

Thom, R., 1972. Stabilité structurelle et morphogénèse: essai d'une théorie générale des modèles. W. A. Benjamin, Reading (Mass.), Etats-Unis d'Amérique.

Tretyakov, M.P., Tretyakova, T.V., Wildemann, V.E., 2021. Influence of the loading system stiffness on the jerky flow in Al-Mg alloy at inelastic and postcritical deformation stages. Procedia Struct. Integr. 33, 1089–1094. http://dx.doi.org/10.1016/j.prostr.2021.10.121.

Valmalle, M., Widell, K., Ilola, R., Bossuyt, S., 2024. DIC analyses and parameter calibration of a strain aging sensitive ductile cast iron. C. R. Méc. 352 (G1), 1–17. http://dx.doi.org/10.5802/crmeca.235.

Van Den Beukel, A., Kocks, U.F., 1982. The strain dependence of static and dynamic strain-aging. Acta Metall. 30 (5), 1027–1034. http://dx.doi.org/10.1016/0001-6160(82)90211-5.

Varadhan, S., Beaudoin, A.J., Fressengeas, C., 2009. Lattice incompatibility and strain-aging in single crystals. J. Mech. Phys. Solids 57 (10), 1733–1748. http://dx.doi.org/10.1016/j.jmps.2009.06.007.

Wang, H., Berdin, C., Mazière, M., Forest, S., Prioul, C., Parrot, A., Le-Delliou, P., 2012. Experimental and numerical study of dynamic strain ageing and its relation to ductile fracture of a C–Mn steel. Mater. Sci. Eng.: A 547, 19–31. http://dx.doi.org/10.1016/j.msea.2012.03.069.

Wendt, H., Abry, P., Jaffard, S., 2007. Bootstrap for empirical multifractal analysis. IEEE Signal Proc. Mag. 24 (4), 38–48.

Wendt, H., Roux, S.G., Abry, P., Jaffard, S., 2009. Wavelet leaders and bootstrap for multifractal analysis of images. Signal Proces. 89 (6), 1100–1114.

Zhang, F., Bower, A., Curtin, W., 2012. The influence of serrated flow on necking in tensile specimens. Acta Mater. 60 (1), 43–50. http://dx.doi.org/10.1016/j.actamat.2011.09.008.

Zhang, S., McCormick, P.G., Estrin, Y., 2001. The morphology of Portevin–Le Chatelier bands: Finite element simulation for Al–Mg–Si. Acta Mater. 49 (6), 1087–1094. http://dx.doi.org/10.1016/S1359-6454(00)00380-3.

Zhu, K.Y., Dai, S., Zou, S.H., Yu, Y.J., Deng, Z.C., 2024. Experimental study and crystal plasticity modeling of additive manufacturing IN718 superalloy considering negative strain rate sensitivity behavior. Eur. J. Mech. A Solids 106, 105304. http://dx.doi.org/10.1016/j.euromechsol.2024.105304.

Zset Software, Z-set | Non-linear material & structure analysis suite. URL: http://www.zset-software.com.